



# ESA CONTRACT REPORT

Contract Report to the European Space Agency

## **Validation of cloud parametrization**

December 2009

*Authors: R. Forbes, M.Ahlgrimm, O. Stiller,  
S. Di Michele and J. Delanoë<sup>1</sup>*

<sup>1</sup>University of Reading

WP-2100 report for ESA contract 1-5576/07/NL/CB:  
Project QuARL - Quantitative Assessment of the Operational  
Value of Space-Borne Radar and Lidar Measurements of Cloud  
and Aerosol Profiles

**European Centre for Medium-Range Weather Forecasts**  
**Europäisches Zentrum für mittelfristige Wettervorhersage**  
**Centre européen pour les prévisions météorologiques à moyen terme**

Series: ECMWF - ESA Contract Report

A full list of ECMWF Publications can be found on our web site under:

<http://www.ecmwf.int/publications/>

Contact: [library@ecmwf.int](mailto:library@ecmwf.int)

©Copyright 2010

European Centre for Medium-Range Weather Forecasts  
Shinfield Park, Reading, RG2 9AX, England

Literary and scientific copyrights belong to ECMWF and are reserved in all countries. This publication is not to be reprinted or translated in whole or in part without the written permission of the Director. Appropriate non-commercial use will normally be granted under the condition that reference is made to ECMWF.

The information within this publication is given in good faith and considered to be true, but ECMWF accepts no liability for error, omission and for loss or damage arising from its use.

Contract Report to the European Space Agency

---

## **Validation of cloud parametrization**

*Authors: R. Forbes, M.Ahlgrimm, O. Stiller,  
S. Di Michele and J. Delanoë<sup>1</sup>*

WP-2100 report for ESA contract 1-5576/07/NL/CB:  
Project QuARL - Quantitative Assessment of the Operational  
Value of Space-Borne Radar and Lidar Measurements of Cloud  
and Aerosol Profiles

European Centre for Medium-Range Weather Forecasts  
Shinfield Park, Reading, Berkshire, UK

December 2009



## ABSTRACT

The current space-borne radar and lidar onboard the CloudSat and CALIPSO satellite missions provide an unprecedented opportunity to evaluate the representation of clouds and precipitation in global atmospheric models and demonstrate the utility of such observations for improvement of NWP and climate models. At ECMWF, the IFS global forecast model is used across a range of resolutions for operational medium-range Numerical Weather Prediction, seasonal forecasting and re-analysis, and appropriate parametrizations are vital for representing the hydrological, radiative and dynamical impacts of cloud and precipitation. This report describes a first evaluation of the ECMWF IFS model with observations from the CloudSat radar and CALIPSO lidar. Different aspects of the model cloud and precipitation fields are investigated with a focus on regional and regime-based statistical comparisons to assess the model and potential improvements to the representation of physical processes. Many of the problems of model-observation comparison due to the different spatial scales in the observations and the model, differences between the parameters observed and prognosed by the model, and uncertainties in the observations are explored, with relevance to both the current active radar/lidar satellite instruments and future missions such as EarthCARE.

## Contents

<b>1</b>	<b>Introduction</b>	<b>1</b>
<b>2</b>	<b>Cloud and precipitation parametrization in the ECMWF forecast model</b>	<b>2</b>
2.1	Description of the parametrization of cloud and precipitation . . . . .	2
2.1.1	Representation of the ice, liquid and the mixed phase . . . . .	2
2.1.2	Representation of sub-grid scale heterogeneity . . . . .	3
2.1.3	Prognostic variables and physical processes . . . . .	4
2.1.4	Convective cloud and precipitation . . . . .	6
2.1.5	Representing boundary layer cloud . . . . .	6
2.2	Discussion of uncertainties, deficiencies and comparison with other schemes . . . . .	7
2.2.1	Comparison with other cloud schemes . . . . .	8
2.2.2	Deficiencies in the current IFS cloud scheme . . . . .	8
2.2.3	New cloud parametrization developments in the ECMWF IFS model . . . . .	10
<b>3</b>	<b>Assessment of ECMWF model with CloudSat/CALIPSO data</b>	<b>13</b>
3.1	Methodology . . . . .	13
3.2	Evaluation of global cloud occurrence . . . . .	15
3.3	Evaluation of forward-modelled radar reflectivity using CloudSat . . . . .	21
3.4	Evaluation of ice water content using a combined radar/lidar technique . . . . .	27
3.5	Evaluation of trade cumulus in the ECMWF model using CALIPSO observations . . . . .	31
3.6	Evaluation of precipitation from low level clouds . . . . .	36
<b>4</b>	<b>Issues and limitations when comparing satellite and model data</b>	<b>37</b>
4.1	Sampling errors (1D vs 2D) . . . . .	37
4.2	Measurement specifications . . . . .	39
4.3	Conclusions and discussion of representativity issues . . . . .	42
<b>5</b>	<b>Conclusions</b>	<b>44</b>
<b>A</b>	<b>List of Acronyms</b>	<b>46</b>

# 1 Introduction

Since 2006 the active radar and lidar on board the CloudSat and CALIPSO satellites have provided an extensive and detailed description of the vertical distribution of clouds and precipitation across the globe. Together with other sensors on-board satellites forming the A-train (OMI on Aura, CERES and MODIS on Aqua, PARASOL), their measurements should help to restrain/constrain the number of free parameters in cloud parametrizations developed for general circulation models (GCMs) of the atmosphere. The representation of cloud is still one of the most uncertain aspects of global climate and Numerical Weather Prediction (NWP) models, with direct or indirect impacts on the hydrological cycle, radiation and atmospheric dynamics. Information on the global distribution of cloud and precipitation vertical profiles from active radar and lidar data has real potential to highlight the deficiencies and compensating errors in these models, with benefits for operational weather forecasting, seasonal forecasting and climate simulation. However, a large number of uncertainties remain as to the best way of producing a meaningful evaluation of the clouds from a GCM. These include the different spatial scales in the observations and the model, differences between the parameters observed and prognosed by the model, and uncertainties and error characteristics of the observations. This report describes the evaluation of aspects of the cloud and precipitation parametrizations in the ECMWF global model addressing many of the issues of representativity and uncertainty associated with the comparison of space-borne radar and lidar observations with numerical models of the atmosphere.

Section 2 provides a brief description of the current cloud and precipitation parametrization scheme in the ECMWF IFS (Integrated Forecast System) model, a discussion of some of the uncertainties and deficiencies of the representation of clouds in GCMs and a brief description of new developments to the parametrization of cloud in the IFS model to address some of these deficiencies.

Section 3 describes an assessment of the ECMWF model with CloudSat and CALIPSO data in terms of global and regional cloud and precipitation properties and different approaches to the model evaluation problem. In particular, there are strengths and weaknesses to both transforms, either from model to observation space (e.g. radar reflectivity), or from observation to model space (e.g. ice water content) and both are explored. As well as an evaluation of different zonal regions, there is a focus on one particular regime, trade cumulus, in which certain physical processes (shallow convection, warm rain microphysics) are dominant. A regime-dependent evaluation can help to identify the source of model deficiencies with the aim of improving the representation of these processes in the model.

Section 4 provides a discussion of issues when comparing satellite measurements with observations based on the representativity work described in QuARL Work Package 1200. Concluding remarks are made in Section 5 regarding the model parametrization evaluation results and the potential for future satellite-borne radar/lidar sensors to further constrain the model parametrization in pursuit of improved performance for climate modelling and Numerical Weather Prediction.

## 2 Cloud and precipitation parametrization in the ECMWF forecast model

In common with other GCMs, the ECMWF global model consists of a dynamical core describing the atmospheric motions discretized to a specified spatial and temporal resolution, and a number of parametrization schemes describing the effects of sub-grid scale physical processes on model predicted quantities represented at the resolved scale (or grid-scale) of the model. These parametrization schemes include radiation, turbulent transport, surface processes, shallow and deep convection, clouds and precipitation (further details can be found in the IFS Documentation; ECMWF, 2009). In this report, the focus is on the parametrization of cloud and precipitation processes and a brief description of the scheme is provided here.

### 2.1 Description of the parametrization of cloud and precipitation

Cloud and “large-scale” (stratiform) precipitation processes are described by prognostic equations for cloud condensate and cloud fraction, with diagnostic relations for precipitation. The basis of the scheme is described in detail in (Tiedtke, 1993), but there are numerous subsequent developments to the scheme including a parametrization of the effects of cloud and precipitation overlap (Jakob and Klein, 2000) and an ice supersaturation scheme (Tompkins *et al.*, 2007). A schematic of the cloud parametrization is shown in Figure 2.1 showing the three moisture related prognostic variables in the model (grid-mean specific humidity,  $q$ , grid-mean cloud condensate,  $l$ , and cloud fraction,  $a$ ) and the diagnostic precipitation for rain and snow. The prognostic cloud fraction variable allows a representation and memory of the sub-grid spatial variability of cloud in each grid-box. There is an underlying probability density function (PDF) associated with the subgrid scale variations of the humidity field (see section 2.1.2) and the functioning of this scheme can be largely understood by considering the impact which the different processes have on this PDF. Various aspects of the cloud scheme are described briefly below, but a more detailed description of the scheme and the physical processes represented in the scheme can be found in the Chapter 6 of the IFS documentation (ECMWF, 2009).

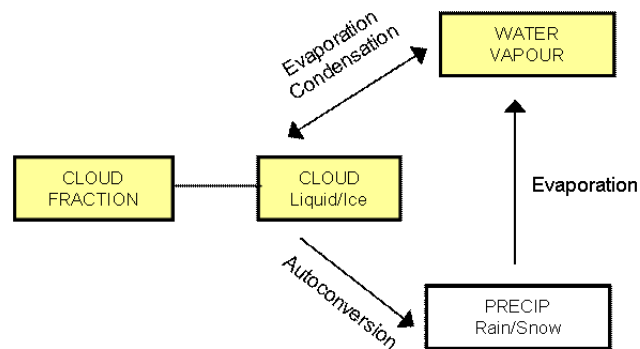


Figure 2.1: Schematic description of the IFS model parametrization of cloud and precipitation with prognostic variables for humidity, cloud condensate and cloud fraction (shaded boxes) and diagnostic variables for rain and snow precipitation (white box).

#### 2.1.1 Representation of the ice, liquid and the mixed phase

There is only one prognostic variable for condensed water,  $l$ , in the current cloud scheme and the distinction between the water and ice phase is determined purely as a diagnostic function of temperature. The fraction,  $\alpha$ , of liquid water in the total condensate is described as

$$\alpha = 0 \quad T \leq T_{\text{ice}}$$

$$\alpha = \left( \frac{T - T_{\text{ice}}}{T_0 - T_{\text{ice}}} \right)^2 \quad T_{\text{ice}} < T < T_0$$

$$\alpha = 1 \quad T \geq T_0 \quad (2.1)$$

where  $T_{\text{ice}} = -23^\circ\text{C}$  and  $T_0 = 0^\circ\text{C}$  define the temperature range in which super-cooled liquid water can exist (i.e. the mixed phase temperature range). Only liquid condensate can exist for temperatures warmer than  $0^\circ\text{C}$ , and only ice for temperatures colder than  $-23^\circ\text{C}$  as illustrated in Figure 2.2. The saturation thermodynamics are calculated according to the mixture of water and ice obtained with (2.1) so that the saturation specific humidity becomes

$$q_{\text{sat}} = \alpha q_{\text{sat}(w)} + (1 - \alpha) q_{\text{sat}(i)} \quad (2.2)$$

where  $q_{\text{sat}(w)}$  and  $q_{\text{sat}(i)}$  are the saturation specific humidities with respect to water and ice, respectively.

Supersaturation with respect to ice is allowed in this scheme for temperatures below  $-23^\circ\text{C}$  following [Tompkins \*et al.\* \(2007\)](#). Ice crystal nucleation contrasts sharply with the equivalent process for liquid cloud droplets, since the nucleation process is not activated at small supersaturation with respect to the ice saturation vapour pressure. Therefore at cold temperatures, where the difference between the liquid water and ice saturation vapour pressures is large, the relative humidity ( $RH$ ) with respect to ice can exceed 150% before the onset of the nucleation process, and supersaturations with respect to ice are commonly observed by in-situ and remote sensing techniques ([Heymsfield \*et al.\*, 1998](#); [Gierens \*et al.\*, 1999](#); [Spichtinger \*et al.\*, 2003](#)).

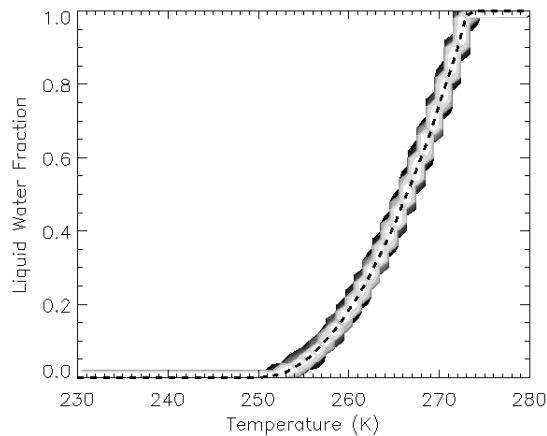


Figure 2.2: Dependence of the relative fractions of liquid and ice condensate on temperature in the cloud parametrization.

### 2.1.2 Representation of sub-grid scale heterogeneity

As mentioned earlier, the representation of the sub-grid scale heterogeneity of water vapour and cloud condensate within a grid-box is based on an underlying PDF of total water. As seen in Fig. 2.3, the employed PDF is split into two parts. Water vapour is assumed to be distributed by a top hat function and is bounded from above by the saturation value  $q_{\text{sat}}$  when there is cloud formation, whilst condensate is represented by a delta-type peak. When the relative humidity is low and there is no cloud formation, the water vapour PDF is given a fixed width determined by a critical relative humidity (currently set to 80% in the mid-troposphere). This defines the grid-mean relative humidity at which cloud will begin to form. The

reasoning for the different treatment of vapour (top-hat PDF) and cloud condensate (delta-function) is based on observations that show there can be considerable spatial variability of humidity, but clouds are generally quite strongly mixed by in-cloud turbulence.

The cloud fraction  $a$  describes the relative partitioning of the gridbox into cloudy and cloud free regions and determines the height of the top-hat humidity PDF by constraining the integral to  $(1 - a)$ . The cloud water content  $l$  determines the position of the delta peak in Fig. 2.3 and the cloud fraction  $a$  determines the height of the peak. As will be seen below, physical processes acting as sources and sinks of cloud and humidity (such as condensation/evaporation) can be formulated in terms of changes to this underlying PDF of total water.

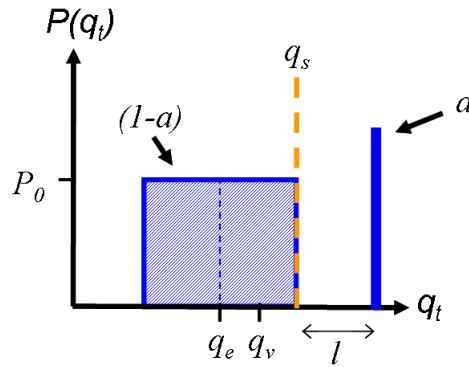


Figure 2.3: Schematic representation of the PDF of total water,  $q_t$ , showing the model sub-grid scale heterogeneity of water vapour and cloud condensate in the cloud parametrization scheme. Vapour is distributed by a top hat function while cloud condensate is represented by the delta type peak at the right of the condensation threshold  $q_s$ . The water vapour value  $q_v$  represents the average over the grid box, while  $q_e$  is the water vapour average over cloud free regions only (the environmental humidity). See text for a further discussion.

### 2.1.3 Prognostic variables and physical processes

The cloud scheme represents the sources and sinks for the grid-box average specific humidity,  $q$ , cloud condensate,  $l$ , and cloud fraction,  $a$ , prognostic variables. The equations for the evolution of these three variables, and for the thermodynamic changes associated with phase changes (dry static energy,  $s$ ) are defined as

$$\frac{\partial l}{\partial t} = A(l) + S_{conv} + S_{strat} - E_{cld} - G_{prec}$$

$$\frac{\partial a}{\partial t} = A(a) + \delta a_{conv} + \delta a_{strat} - \delta a_{evap}$$

$$\frac{\partial q}{\partial t} = A(q) - S_{strat} + E_{cld} + E_{prec}$$

$$\frac{\partial s}{\partial t} = A(s) + L[S_{strat} - E_{cld} - E_{prec}] - L_{fus}M + c_p \{(1 - a)R_{clear} + aR_{cld}\}$$

The terms on the right-hand side represent the following processes:

1.  $A(l), A(a), A(q), A(s)$  – transport (advection) of cloud condensate, cloud fraction and humidity through the boundaries of the grid volume.

2.  $S_{\text{conv}}, \delta a_{\text{conv}}$  – formation of condensate and cloud fraction by convective processes (detrainment)
3.  $S_{\text{strat}}, \delta a_{\text{strat}}$  – formation of cloud condensate and cloud fraction by stratiform condensation processes. (i.e.  $\frac{d}{dt}q_{\text{sat}} < 0$ )
4.  $E_{\text{cld}}, \delta a_{\text{evap}}$  – evaporation of condensate by large scale forcing (i.e.  $\frac{d}{dt}q_{\text{sat}} > 0$ ) and of condensate and cloud fraction by turbulent mixing
5.  $G_{\text{prec}}, E_{\text{prec}}$  – generation and evaporation of precipitation
6.  $M, R_{\text{clear}}, R_{\text{cld}}$  – melting rate, clear sky radiative heating and cloud radiative heating respectively

where  $q_{\text{sat}}$  is the saturation value of the specific humidity defined by Eq. (2),  $L$  and  $L_{\text{fus}}$  are the latent heats of condensation and fusion respectively, and  $c_p$  is the specific heat capacity of water.

Cloud formation occurs through processes 2 and 3; convection and stratiform cloud formation. Clouds formed by convective processes are parametrized by considering them to be condensate produced in cumulus updraughts and detrained into the environmental air. This approach, besides being part of the cloud parametrization, represents an important extension of the model's cumulus parametrization and is applied for all types of convection (deep, shallow and mid-level). The convective detrainment process acts to increase both cloud fraction  $a$  and condensate  $l$  accordingly.

The formation of clouds by non-convective processes (e.g. large-scale lifting of moist air, radiative cooling) is based on the principle that condensation processes are determined by the rate at which the saturation specific humidity decreases. So, large scale cloud formation is activated for  $\frac{d}{dt}q_{\text{sat}} < 0$  if the relative humidity  $RH$  exceeds a critical value  $RH_c$ . This cloud formation process can be fully described by the PDF shown in Fig. 2.3, where  $RH_c$  determines the initial width of the humidity PDF before the onset of condensation. While the saturation value  $q_{\text{sat}}$  is shifted to the right (i.e.  $\frac{d}{dt}q_{\text{sat}} < 0$ ), the height  $P_0$  of the unsaturated part of the PDF is conserved (in a Lagrangian sense) during the process. Changes to the position of the delta peak for  $l$  follow directly from the conservation of total water, while the magnitude of the peak is constrained by the fact that the PDF has to be normalized.

The evaporation by large scale forcing ( $\frac{d}{dt}q_{\text{sat}} > 0$ ) on the other hand leaves  $a$  unchanged (apart from situations where all the liquid water is evaporated for which  $a$  is set to zero). Apart from convection induced subsidence (which redistributes  $a$  and  $l$  in the vertical), the only process which decreases  $a$  (in a Lagrangian sense) is turbulent mixing. Turbulence can evaporate cloud condensate  $\delta l_{\text{turb}}$  while the cloud fraction is adjusted to conserve the in-cloud condensate  $l/a$ . The amount of condensate which evaporates is directly proportional to the vapour saturation deficit (i.e.,  $\delta l_{\text{turb}} \propto (q - q_{\text{sat}})$ ). This amount is generally small, but can become important for removing clouds whose condensate has been largely eroded by precipitation and/or large scale evaporation.

A major role for the reduction of cloud condensate (and thus the life time of a cloud) is played by the microphysics which governs the generation of precipitation,  $G_{\text{prec}}$ . The autoconversion rates of liquid to rain (Sundqvist *et al.*, 1989) and ice to snow (Lin *et al.*, 1983) are defined as functions of the amount of in-cloud condensate (and temperature for the ice phase). While the initial formation of precipitation is due to an auto conversion process, a dominant role at later stages is usually played by collection processes. Since the hydrometeors are treated only diagnostically, collection processes have also been included in a purely diagnostic fashion. More precisely, the autoconversion rate (or precipitation efficiency) is increased in places where precipitation is already falling through the cloudy part of a grid box. A similar treatment has been adopted for the Bergeron-Findeisen mechanism which enhances precipitation in the temperature range where this mechanism is assumed to be activated. Melting of snow precipitation occurs as it falls through the freezing level.

The evaporation of precipitation,  $E_{\text{prec}}$ , is an important process as precipitation can often fully or partially evaporate before it reaches the surface, and is proportional to the saturation deficit. The process also increases  $q_v$  and a source term therefore has to be included in the humidity equation. Evaporation tends to decrease the width of the vapour subgrid fluctuations.

In situations with partial cloud cover ( $0 < a < 1$ ), collection processes and the evaporation of precipitation depend on which portion of the total precipitation is falling through cloudy and non-cloudy regions, respectively (Jakob and Klein, 2000). At present, the precipitation process assumes maximum-random overlap of clouds in the vertical.

With the processes described above, a typical life cycle of a cloud simulated by this scheme can be described as follows.

- First the cloud is formed through large scale forcing ( $\frac{d}{dt}q_{\text{sat}} < 0$ ) or convective detrainment.
- Then the condensate is decreased through precipitation and possibly large scale forcing ( $\frac{d}{dt}q_{\text{sat}} > 0$ ), both of which leave the cloud fraction invariant. The efficiency of the precipitation formation can be strongly influenced by ice micro-physics.
- When the condensate is sufficiently eroded the cloud fraction (and what is left from the cloud condensate) is destroyed through turbulent evaporation.

#### 2.1.4 Convective cloud and precipitation

The above section describes the prognostic cloud scheme and the stratiform precipitation. Cumulus convection is parametrized separately by a bulk-mass flux scheme described in Tiedtke (1989a) and Bechtold *et al.* (2004). The scheme considers deep, shallow and mid-level convection. Convective clouds are represented by a single pair of entraining/detraining plumes which describe the updraught and downdraught processes. Entrainment rates are defined by a vertical scaling function together with a relative humidity based organized entrainment (since IFS cycle CY32R3 introduced in 2007), and a variable convective adjustment time-scale, a combination which enables the model to maintain a realistic level of tropical variability (Bechtold *et al.*, 2008). An important component of the IFS model is the link between the convection parametrization and the cloud scheme. The convection scheme determines the condensation rate in the convective cores (which are assumed to cover only a small part of the grid box) but then detrains cloud directly into the prognostic cloud fraction and condensate variables. Thus, although the model has no explicit cloud associated with the convective cores, it does have a memory of the detrained convective cloud in the two prognostic variables, particularly important for representing convective anvils with a decay timescale much longer than the timestep of the model. As for convective precipitation, the convection parametrization does generate its own rain and snow from the convective cores, with very similar precipitation microphysics to the stratiform scheme in terms of autoconversion, melting and evaporation. Chapter 5 of the IFS Documentation (ECMWF, 2009) describes the parametrization of convection in much more detail.

#### 2.1.5 Representing boundary layer cloud

Low level cloud such as stratocumulus and shallow cumulus are very much tied to the representation of turbulent and convective processes in the boundary layer, with scales of motion ranging from very small turbulent motions that dissipate energy to large overturning convective circulations. This range of scales is not resolved in a NWP model, so the boundary layer transport must be parametrized. The convective motion in the boundary layer can lead to the formation of clouds, yet in many models, the turbulent motions

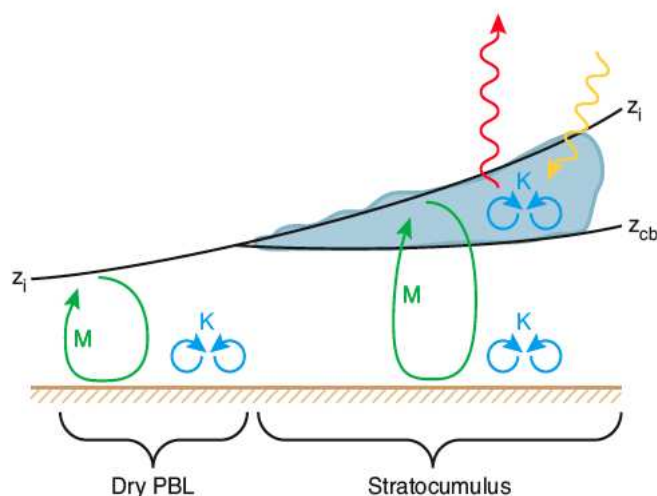


Figure 2.4: Schematic representation of the transition of a dry boundary layer to stratocumulus. The parametrization of the associated convective transports in the EDMF scheme are illustrated in blue for the diffusion component and in green for the mass-flux component.

of the boundary layer are treated as distinct from boundary layer clouds, using separate parametrizations. The IFS is being developed towards a unified treatment of boundary layer and boundary layer clouds and a first step towards this was the introduction of the Eddy Diffusivity Mass Flux (EDMF) parametrization in IFS version CY29R1 in 2005. This parametrization explicitly models large convective overturning motions using the mass flux concept, while small scale turbulence is treated through K-diffusion (Köhler, 2005; Tompkins *et al.*, 2004). The top 10% of the vertical velocity distribution in the boundary layer is chosen to be represented directly with a mass flux. Moist-conserved variables are used, such that the saturation state of the convective updraught is known. Thus, the EDMF parametrization creates cloud when the updraught reaches the lifting condensation level (Fig. 2.4). In areas with large low-level stability, such as the marine stratocumulus regions, the EDMF scheme is allowed to create clouds. This has substantially improved stratocumulus cover in the IFS (Köhler, 2005; Ahlgrimm *et al.*, 2009). In areas with less low-level stability, such as the trade cumulus regions, the clouds at the lifting condensation level continue to be treated with the modified Tiedtke parametrization for shallow convection (Tiedtke, 1989a). The recent extension of the EDMF scheme to also represent shallow convective transport and cloud formation is described in section 2.2 below.

## 2.2 Discussion of uncertainties, deficiencies and comparison with other schemes

Parametrization schemes are approximations of the real physical processes occurring in the atmosphere and their formulation is limited by (a) our understanding of the processes, (b) how to represent them in a discretized system and (c) available computational resources. There will always be some level of uncertainty, but what is important is that the degree of approximation in the parametrization formulation is appropriate for both our current knowledge of the process and the particular model system in which the parametrization is being used. The parametrization of cloud and precipitation in the ECMWF global model needs to be appropriate to describe the processes at the spatial and temporal resolutions it is currently used for (of order 10-100km grid lengths), but with no more degrees of freedom than can be understood or constrained with observations. This sub-section compares the ECMWF cloud scheme with a range of schemes used in GCMs and discusses some of the main deficiencies and uncertainties where improvements could be made.

### 2.2.1 Comparison with other cloud schemes

It is useful to place the current ECMWF parametrization of cloud and precipitation processes in context within the hierarchy of other schemes used in climate and weather forecasting numerical models. The simplest scheme has only water vapour as a prognostic and does not explicitly represent clouds, but generates precipitation by removing any supersaturation in the atmosphere. The [Sundqvist \(1978\)](#) scheme has only prognostic water vapour but does treat cloud diagnostically by again assuming any supersaturation leads to condensation. In this scheme precipitation is modelled by instantaneously removing a part of the condensate produced by the cloud scheme. In the [Smith \(1990\)](#) scheme, one prognostic variable is used to represent water vapour, cloud liquid water and cloud ice. The water vapour and condensate are combined to form a total water prognostic variable that is advected, and the vapour/condensate re-partitioning is performed diagnostically each timestep. The condensate is either liquid or ice or a mixture dependent on the temperature. Precipitation is treated diagnostically and is either rain or snow, dependent on temperature. The Smith scheme assumes that there is no ice supersaturation in the atmosphere in order to calculate the partitioning. This assumption is less valid than the assumption for water as significant ice supersaturations are commonly observed. The ECMWF scheme based on [Tiedtke \(1993\)](#) is a step further in complexity by including an additional prognostic equation for cloud fraction as well as condensate, in addition to allowing the occurrence of ice supersaturation.

Many parametrization schemes separate the representation of ice phase and liquid phase cloud with two or more prognostic variables giving additional degrees of freedom for mixed phase cloud evolution. The [Wilson and Ballard \(1999\)](#) parametrization scheme is an example of such a scheme which has a prognostic variable for liquid cloud and one for the ice phase, that represents the range of ice particles from cloud ice crystals to precipitating snowflakes. Other schemes such as split frozen water into two prognostics representing separately the cloud ice and falling snow. More complicated parametrizations represent ice particle size spectra with two prognostic variables, the mass mixing ratio and number concentration (double moment schemes) ([Ferrier 1994](#); [Ikawa et al. 1991](#); [Wang and Chang 1993](#); [Ghan et al. 1997](#); [Swann 1998](#)). Such schemes are more computationally expensive and are generally only used in numerical models in research mode, but for example [Ghan et al. \(1997\)](#) showed that the ice-number concentration was an important factor in determining the climate of their model. Most schemes treat rain diagnostically although some (e.g. [Fowler et al. 1996](#)) have a prognostic variable for rain. The more complex bulk-microphysical parametrizations used in high resolution numerical models for convective scale studies include a further prognostic variable representing graupel and/or hail ([Lin et al. 1983](#); [Walko et al. 1995](#); [Swann 1998](#)). Multi-moment schemes or bin-microphysics schemes which explicitly represent the particle size distributions with discrete “bins” are generally only used for research in high resolution models.

In summary, there are a wide variety of microphysical schemes in use varying from simple diagnostic to complex prognostic schemes, but for a particular application, there needs to be a balance between the sophistication of a microphysics scheme and the resolution of the numerical model. Microphysics is generally controlled by mesoscale to convective scale dynamics with updraughts of order 0.1 to 1 m/s. If a model cannot resolve the appropriate scale of the dynamical forcing, then a sub-grid scale parametrization is required that attempts to take account of the mismatch between the dynamics produced by the model and the dynamics that the cloud microphysics parametrization requires. Few, if any, actually represent the sub-grid dynamics explicitly. The key point is that the microphysics should be formulated at a level of complexity that is appropriate for the model.

### 2.2.2 Deficiencies in the current IFS cloud scheme

As can be seen from the above discussion, the current IFS cloud scheme based on [Tiedtke \(1993\)](#) lies in the mid-range of the parametrization hierarchy in terms of microphysics complexity, but the prognostic

representation of cloud fraction with parametrized sources and sinks was relatively advanced for its time and has performed well in the ECMWF global NWP model for many years. With increasing availability of new cloud observations, improved understanding of how to represent microphysical processes in numerical models, increasing computational resources and higher model resolutions, some of the approximations made in the Tiedtke (1993) scheme have become less valid over time. In particular, there are a number of aspects that could be improved:

*i) Diagnostic treatment of the fraction of ice/liquid in mixed phase cloud*

The average occurrence of super-cooled liquid water decreases with height (temperature) and a first approximation is to specify a simple function of temperature that represents this decrease to give the correct average super-cooled liquid water occurrence in the model (Hogan *et al.*, 2003). However, the mixed phase cloud occurrence varies with geographical region, meteorological regime and individual cases, with super-cooled liquid water often in isolated regions or in thin cloud layers (e.g. altocumulus)(Hogan *et al.*, 2004). Changing to separate ice and liquid prognostic variables with an appropriate representation of mixed-phase processes should enable the model to capture some of the variability in the occurrence of super-cooled liquid water that is observed in the atmosphere.

*ii) Diagnostic representation of precipitation*

A diagnostic representation of precipitation assumes a separation of timescales between the timestep of the model and the time it takes for the precipitation to fall from cloud to ground. For a low resolution model with a timestep of order of an hour, this is a good assumption for rain and a reasonable assumption for snow. This enables the representation of an equilibrium profile of the precipitation flux generated in the model each timestep independently in each grid column. However, as the model spatial resolution becomes smaller and the timestep shorter, the approximation becomes less valid. Precipitation, particularly the slower falling snow, can take significantly longer than the timestep of the model to fall from cloud to ground and could be advected by the wind considerable horizontal distances. A prognostic representation of snow (and to a lesser extent rain) therefore becomes increasingly important.

*iii) Representation of hydrometeor particle size distribution, characteristics and microphysical processes*

Many of the source and sink terms for the cloud/precipitation variables are based on different assumptions about the underlying microphysical properties, particularly for the ice phase, and some have no clear relationship. The process rates depend on the particle size distribution and particle characteristics (e.g. assumed ice particle shape, density and fall speed). There is therefore potential to improve the underlying physical basis of the microphysics by formulating the process rates in terms of a common and consistent set of microphysical properties based on observational data.

*iv) Representation of sub-grid inhomogeneity of temperature, humidity, cloud and precipitation*

There is heterogeneity in atmospheric temperature, humidity and cloud at all scales and one role of the cloud scheme is to represent this variability on the sub-grid scale. The prognostic cloud fraction formulation in the IFS represents an underlying PDF of humidity as a top-hat function and a well mixed cloud within a grid box, with a number of *ad hoc* assumptions for the sources and sinks of cloud fraction. However, observations of the spatial variability of humidity (e.g. from aircraft or Raman lidar) show a more Gaussian-like

distribution with positive or negative skewness. Hence researchers have investigated other statistical cloud scheme formulations to represent the heterogeneity in a more realistic way with sources and sinks directly changing the shape of the function (e.g. Tompkins, 2002). It is desirable to move to a more physical basis, representing sub-grid inhomogeneity of humidity and other variables such as temperature, cloud condensate and precipitation in a more realistic way. These variations are often forced by small-scale vertical wind perturbations and how to represent the microphysical forcing by small-scale and turbulent dynamics (e.g. in stratocumulus or cirrus) remains a major issue for representation in global scale models.

*v) Interactions of cloud and precipitation with radiation and dynamics*

There is still considerable uncertainty relating to the interactions between cloud, aerosol, precipitation and radiation. The assumed particle size distributions of both liquid and ice cloud can have a significant impact on radiation (e.g. smaller effective radius leads to increased reflection of short-wave radiation) with consequences for both global and local radiative heating/cooling rates and associated circulation changes. Cloud-aerosol-radiation-precipitation interactions are significant areas of ongoing research in the field of global modelling for both NWP and climate prediction.

How to improve the parametrization of cloud and precipitation to address the above issues is not always clear, and observations remain a vital part of the development process. Data from space-borne active radar and lidar certainly have the potential to help with some of the above and later in the report a first assessment of the impact of the model developments relating to (i) and (ii) are presented for the ice phase. The recent changes to the cloud scheme are briefly discussed below. In addition, an extension of the formulation of the boundary layer scheme to represent shallow cumulus is described as another recent model development that is evaluated later in the report.

### *2.2.3 New cloud parametrization developments in the ECMWF IFS model*

#### **(a) New prognostic cloud microphysics scheme**

A new version of the cloud microphysics scheme is currently being developed to address the first two deficiencies highlighted in section 2.2.2 above; the diagnostic treatment of the fraction of ice and liquid cloud and the diagnostic representation of precipitation. The two main changes are:

- The constraint of the liquid/ice condensate fraction dependency on temperature is removed. The liquid water content and ice content are now allowed to vary independently of temperature, introducing an extra degree of freedom into the scheme.
- The precipitation variables, rain and snow, are changed from a diagnostic to a prognostic representation. The new scheme contains separate equations for the temporal and spatial evolution of both variables and includes advection by the dynamics.

A schematic of the new scheme is shown in Fig. 2.5 and can be compared to the current scheme in Fig. 2.1. Additional microphysical process rates relevant to the split of the cloud water from the cloud ice variable have been included and a wide distribution of different liquid and ice fractions are now possible across a range of temperatures (Fig. 2.6). The changes affect all of the sources and sinks in some way, particularly those processes that depend on the relative humidity as the new scheme represents both saturation with

respect to liquid water and with respect to ice rather than a single hybrid function (Eq. 2). The Bergeron-Findeison mechanism is represented explicitly with evaporation of supercooled liquid water droplets and deposition onto ice particles in air that is subsaturated with respect to water but supersaturated with respect to ice. The new precipitation prognostic variables are now represented as mass fields, rather than flux fields, and both rain and snow are taken into account in the density of moist air in the new scheme with the potential to affect the flow dynamics. In addition the snow field is included in the radiation parametrization. As the snow represents a significant part of the total ice water path in the atmosphere, it is important to include this in any evaluation of the ice phase. The new scheme is evaluated in Section 3.4 against ice water content derived from observations.

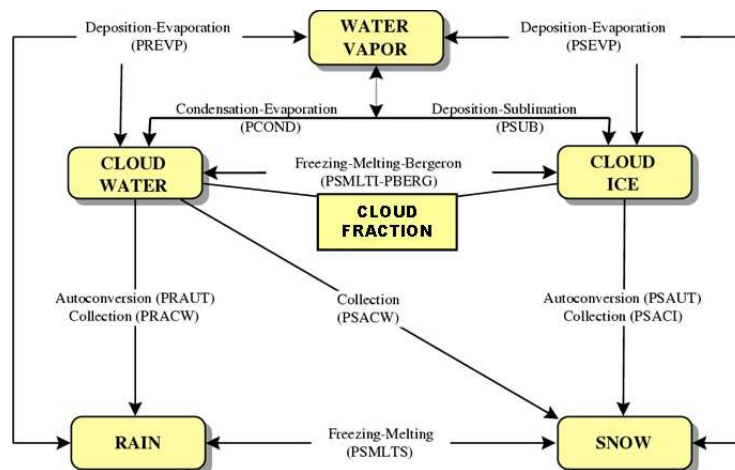


Figure 2.5: Schematic of the new cloud and precipitation parametrization being developed for the IFS model with prognostic variables for humidity, cloud liquid, cloud ice, rain, snow and cloud fraction.

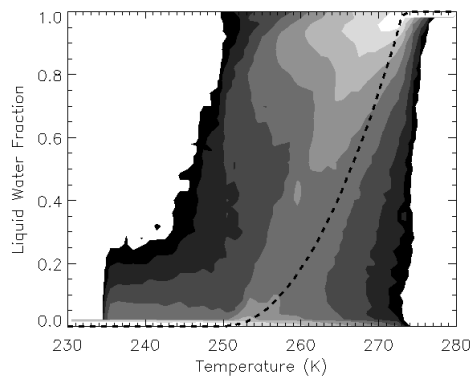


Figure 2.6: Distribution of the relative fractions of liquid and ice condensate for a range of temperatures in the new cloud parametrization scheme. The diagnostic temperature function used in the current scheme is shown as a solid line.

### (b) Unified approach to boundary layer turbulence, cloud and shallow convection

In an effort to treat all boundary layer convection within one framework, the EDMF scheme (described briefly in section 2.1.5 above), has been extended further into the Dual Mass Flux parametrization (DualM). Instead of one explicit updraught with fixed width, which can be either clear or cloudy, the DualM parametrization allows two updraughts, one dry and one moist (described in detail in [Neggers \*et al.\*, 2009](#); [Neggers,](#)

2009). The total updraught fraction is still fixed, but the subdivision into dry and moist updraughts is smoothly variable (Fig. 2.7). This parametrization can represent the full range of completely cloudy updraughts (such as found in the stratocumulus regime), through partially cloudy (trade cumulus), to completely dry updraughts (such as a dry convective boundary layer) and is undergoing a process of evaluation in the IFS model. Although the DualM scheme aims to replace the Tiedtke (1989b) formulation for surface driven shallow cumulus, the Tiedtke parametrization is still used for deep and mid-level convection, and for shallow convection that originates above the surface layer. In section 3.5, trade cumulus cloudiness in the IFS is evaluated for model versions using the EDMF and DualM parametrizations.

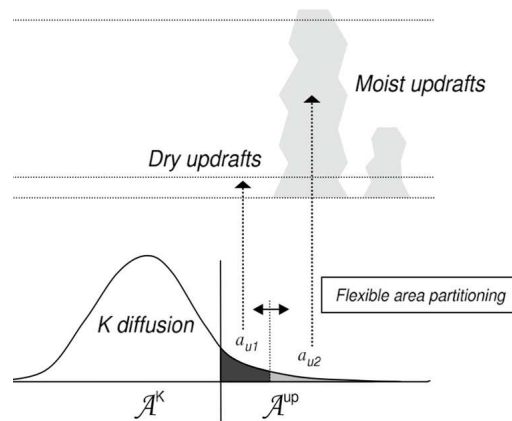


Figure 2.7: Schematic representation of the DualM scheme showing the separate dry and moist updraughts.

## 3 Assessment of ECMWF model with CloudSat/CALIPSO data

### 3.1 Methodology

A prerequisite for the model-observation comparison is an appropriate transform, either from model to observation space (“model-to-obs”), or from observation to model space (“obs-to-model”), in order to compare “like-with-like”. These transforms need to take account of not only the different parameters observed and prognosed by the model, but also the different spatial scales in model and observations, and uncertainties and error characteristics of the observations. If these differences are not understood or dealt with appropriately, then the model evaluation can lead to misleading results. The following discussion describes the methodologies for comparing the IFS with CloudSat and CALIPSO:

#### *(i) Comparing model and observed parameters*

One option is to use a forward operator to process model output in terms of the CloudSat and CALIPSO-derived parameters (radar reflectivity factor and lidar backscatter). The focus of Work Package WP1000 was to develop an appropriate forward model for radar reflectivity, assessing the CFMIP community simulator (COSP, [www.cfmip.net](http://www.cfmip.net)) and the ECMWF radar reflectivity operator (ZmVar). These forward models calculate the attenuated radar reflectivity for the 94GHz CloudSat radar from the model stratiform and convective cloud and precipitation fields and are discussed in detail in the WP1000 report. An evaluation of the model derived reflectivity is described in Section 3.3 below. There are a number of assumptions regarding the model hydrometeor particle size distributions and particle characteristics that need to be made, which should be consistent with the assumptions in the model. There is, however, some ambiguity whether the source of reflectivity differences is from the amount of condensate prognosed by the model or from the microphysical assumptions that are used for the forward model. It is therefore also of interest to follow the obs-to-model approach to validation provided by CloudSat Level-2 products (cloud mask and estimates of cloud phase and water contents) or alternative algorithms (e.g. [Delanoë and Hogan, 2009](#)). An example of deriving ice water content (IWC) from the radar alone and from a combination of data from different instruments to compare directly with the ice/snow prognostic fields in the model is given in section 3.4. There are still assumptions that need to be made in estimating the model quantity from the observations, but one way of reducing the chance of mis-interpreting any results and providing more confidence in a model evaluation is to approach the problem from different angles with a different and independent set of assumptions.

#### *(ii) Appropriate spatial and temporal matching*

There are a number of aspects to the problem of matching the spatial and temporal scales of model and observations. For the A-Train, it is appropriate to extract the model data along the satellite track at the appropriate time (the model data used here is matched with the CloudSat and CALIPSO track and is always within 1.5 hours of the observation time).

Secondly, there is the need to address the mismatch in spatial scales in the model (50 km) and observations (1 km). Sub-grid variability is predicted by the IFS model in terms of a cloud fraction and assumption of the vertical overlap of cloud. There are two approaches to overcome this problem:

- (1) Average obs to a model representative spatial scale (the grid scale).
- (2) Statistically represent model sub-gridscale variability using a cloud generator.

These two options are shown schematically in Figure 3.1. In option (2), the sub-grid scale distribution of cloud elements and vertical overlap is represented by the cloud generator of Räsänen *et al.* (2004). Recently the same cloud generator was implemented in the IFS radiation scheme in combination with the Monte-Carlo Independent Column Approximation in an attempt to deal with the sub-grid cloud problem (Morcrette *et al.*, 2008). The sub-grid cloud generator approach has the advantage that it is able to better represent the impact of attenuation in the model calculated radar reflectivity and it is this approach that is used in Section 3.3 (also discussed in more detail in the QuARL WP1000 report.) An example of the cloud averaging approach (option 2 above) can be found in Section 3.4 for the ice water content comparison.

A statistical approach to model validation needs to have a large enough data sample to be robust. Statistics may vary due to regional variations (e.g. tropics, mid-latitudes, high latitudes), regime dependent variations (fronts, convection, stratocumulus, trade cumulus), seasonal variations and interannual variations. For a global dataset, a day of observations (14 orbits) is generally representative and highlights the robust differences between model and observations. However, for smaller regions, a longer timeseries is required as the number of tracks crossing the region can be small. A few weeks or a month of data provides robust statistics for the regions used for the results in this section. Representativity errors relating to the statistical sampling and the fact that CloudSat and CALIPSO sample a narrow (1D) track (of order 1 km) compared to the model 2D grid boxes is discussed in more detail in Section 4.

### *(iii) Observation error characteristics and limitations*

Observations have associated error characteristics, but also limitations in what they can observe. There are a number of points that are worth highlighting regarding the different information that can be extracted from the CALIPSO lidar and from the CloudSat radar:

The CALIPSO lidar is most sensitive to small particles (backscatter is proportional to particle diameter squared,  $D^2$ ), so the lidar is dominated by a return from cloud droplets and small ice particles, making it particularly useful for water clouds and thin cirrus. The backscatter signal is quickly attenuated by small water droplets and often only sees the top of water cloud, obscuring precipitation and cloud layers lower in the atmosphere.

The CloudSat radar is more sensitive to large particles (reflectivity  $\propto D^6$ ) and is therefore dominated by precipitation as well as cloud containing larger particles. However, the radar can miss cloud with small particles such as thin cirrus and many liquid water clouds. The radar provides profile information at an effective 500m resolution down to an altitude of about 750m above the ground (range gates lower than this are contaminated with a strong backscatter signal from the surface). It is possible to identify rain from the CloudSat signal due to the significant difference in particle size distributions between cloud droplets and rain drops, but the ice phase is characterised by a more continuous spectrum of particle sizes and there is no clear distinction between cloud ice and precipitating snow particles.

The radar and lidar data sources are to a large extent complementary so a combined product has the potential to give a more complete picture of the occurrence of hydrometeors as well as water contents and other properties of cloud and precipitation. For the obs-to-model approach, both the GEOPROF-LIDAR product and the combined radar/lidar product developed at the University of Reading (Delanoë and Hogan, 2009) are examples of this. In the model-to-obs approach, the forward model has assumptions built in to emulate the observation limitations (i.e. radar not seeing small particles, attenuation, sensitivity threshold of around -30dBZ)

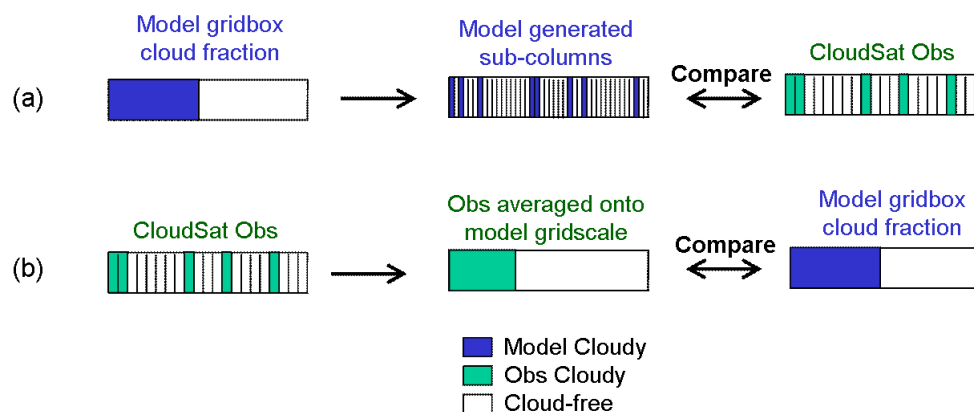


Figure 3.1: Schematic representation of two approaches to addressing the spatial scale mismatch between the high resolution CloudSat (or CALIPSO) observations and lower resolution model; (a) using a cloud generator on the model cloud fraction field to produce sub-columns representing the high resolution of the observations, (b) averaging the high resolution observations to the lower resolution model grid.

## 3.2 Evaluation of global cloud occurrence

The first evaluation of the model performance is to assess the global distribution of cloud and precipitation (i.e. hydrometeors). There are several hydrometeor occurrence products derived from CALIPSO, CloudSat or a combination of the two and this section compares the different products with each other and with the IFS model. Each product is described in turn below with the zonal average cross sections of hydrometeor frequency of occurrence for January and July 2007 shown in Figs. 3.3, 3.4 and 3.5.

### (a) CALIPSO only product

The vertical and horizontal resolution of the backscatter observed by CALIPSO varies with height. Features higher up in the atmosphere tend to have lower optical depth and are harder to distinguish from background noise. Above 8.3 km, three individual profiles, spaced 333 m apart, are averaged together to increase the signal-to-noise ratio. Above 22 km, 15 individual shots are averaged along a 5 km section of the track. The vertical bin size varies from 30 m below 8.3 km over 60 m in the upper troposphere to 120 m above 22 km.

Two types of level 2 cloud products are available: the vertical feature mask (VFM), and cloud layer products at three resolutions (333 m, 1 km, 5 km; examples shown in Fig. 3.2a,b,c). In the VFM, each horizontal and vertical bin is reported separately and flagged for cloud. The detection algorithm searches for features at single shot (333 m) resolution, 1 km, 5 km 20 km and 80 km horizontal averaging. If a bin is cloudy, a flag is set to mark how much averaging was necessary to detect the cloud (Fig. 3.2d). If profiles have to be averaged over long distances, the detected layer will still have only one base and top height, which is reported for the full 20 km or even 80 km. This leads to unrealistically “blocky” clouds, as evident in the blue and green colour in the figure. The actual observed backscatter is shown in Fig. 3.2e for comparison.

The cloud layer products report the same information, but use much less data volume. Only the number of detected layers, and each layer’s base and top height are reported, together with some quality flags. In the 333 m and 1 km layer products, only those clouds detected at the respective resolutions are reported in the product. Any clouds that needed averaging over 5km or more are excluded. For the 333 m product, this means that all clouds above 8.3 km are missing. The 1km product will miss some of the very optically thin clouds. The 5 km layer product reports all clouds found in the VFM, including the somewhat unrealistic looking clouds detected with 80 km averaging.

For the figures shown here (Fig. 3.3, first row), the 1 km cloud layer product was used for the cloud mask. It may miss some tenuous clouds, but will not introduce any unrealistically large amount of high clouds through the blocky features in the 5km product. For each reported lidar shot, a binary cloud profile at 1 m vertical resolution based on the detected cloud base and top height was created. All binary profiles falling into a one-degree latitude wide bin were then averaged for the frequency of cloud occurrence. The vertical resolution was down-graded to 10 m before plotting.

An inherent limitation of the lidar is the rapid signal attenuation in optically thick (optical depth  $> 3$ ) clouds. Since all optically thick clouds are missed by the lidar, the cloud occurrence is much lower than for the other cloud masks shown. Careful examination also shows a detection threshold at 8.3 km. The difference in the background noise level above and below this height is evident in Fig. 3.2e.

#### *(b) CloudSat only product*

The CloudSat radar detects particles above a certain size limit, including cloud ice and liquid particles, as well as various forms of precipitation. While rain and cloud droplets generally have quite distinct sizes and can be separated according to the radar reflectivity, the size of cloud ice particles transitions smoothly into precipitating ice. A mask based on radar reflectivity therefore includes both cloud and precipitation. Since precipitation particles are generally larger, the strength of the reflectivity is dominated by precipitation. Particles below a given size threshold, such as small ice particles or non-precipitating liquid clouds with small droplets, may be missed by the radar. Within the lowest 500-1000m, the radar's signal is impaired by ground clutter and detection of hydrometeors is unreliable.

The cloud mask shown in the Fig. 3.3, second row, is based on the level 2 CloudSat GEOPROF product. It reports the likelihood that each vertical bin (approx. 240 m) is filled with cloud. We have chosen to consider the bin cloudy when the cloud mask flag has a value between 20 and 40. Not surprisingly, the reported cloud and precipitation occurrence in the GEOPROF product is significantly greater than in the CALIPSO product, due to the much weaker attenuation of the radar signal. However, the lidar detects more cirrus clouds near the tropopause than the radar.

#### *(c) Combined CloudSat/CALIPSO GEOPROF-Lidar product*

The GEOPROF-Lidar product uses both radar and lidar observations to provide a combined cloud and precipitation mask. The contribution from CALIPSO is based on the VFM and the contribution from CloudSat is based on the GEOPROF cloud mask flag (Level 2 Radar-Lidar GEOPROF Product Version 1.0, Process Description and Interface Control Document). All the points discussed for the separate data products also apply for the combined product. In particular, the 8.3km detection threshold from the lidar is also apparent in the combined product, most notable over the winter poles.

#### *(d) Combined CloudSat/CALIPSO University of Reading product*

The University of Reading product is based on the same CloudSat and CALIPSO VFM products, but uses the lidar backscatter and radar reflectivity to refine the VFM. If the lidar's backscatter does not exceed the molecular backscatter (calculated from the model pressure, humidity and temperature), the pixel is considered to be non-cloudy, despite the VFM's initial labelling. Also, features marked as aerosol in the VFM that have a corresponding radar reflectivity are re-labelled as cloud. This removes some of the blocky clouds only detected through extensive horizontal averaging, and corrects mis-labelling that occasionally occurs between thin ice clouds and aerosol features. Compared to the GEOPROF-Lidar product, the Reading

University cloud mask shows slightly less cloud cover overall, and a less pronounced detection threshold at 8.3km. Differences also exist in the ground clutter region near the surface.

*(e) ECMWF Model*

The IFS is initialized at 12UTC every day, and three-hourly output from forecast hours 12 to 36 is stitched together to provide a continuous record of model data. The model data are extracted along the satellite track. For each model grid point, 20 subcolumns are generated using the maximum-random overlap assumption for cloud cover and precipitation fluxes. A radar forward model (ZmVar) is run on the subcolumns. The levels of each subcolumn with a radar reflectivity above -30dBZ (approximate sensitivity threshold of the CloudSat radar) are considered to be “cloudy”. In addition, all levels with cloud in the subcolumn are considered to be cloudy. This is not strictly the same as running a lidar forward model on the subcolumns. However, unless artificial noise is added to the molecular background backscatter in the forward model, levels with simulated backscatter above the background are identical to those with cloud cover.

Individual subcolumns are treated like lidar or radar observations and recast onto a regular height grid. Figure 3.4, bottom row, shows that the model has cloud/precipitation more frequently in the mid-latitudes, particularly the boundary layer, as well as in the equatorial mid-troposphere. Figure 3.5 shows masks based on only the model’s cloud cover variable (left panel) and only the precipitation flux (right panel) for the month of July 2007. Clearly, the very high occurrences in the southern hemispheric mid-latitudes are linked with precipitation events. Also noteworthy are the high cloud and precipitation occurrences at low levels near the north pole. Neither CALIPSO nor CloudSat observe these clouds.

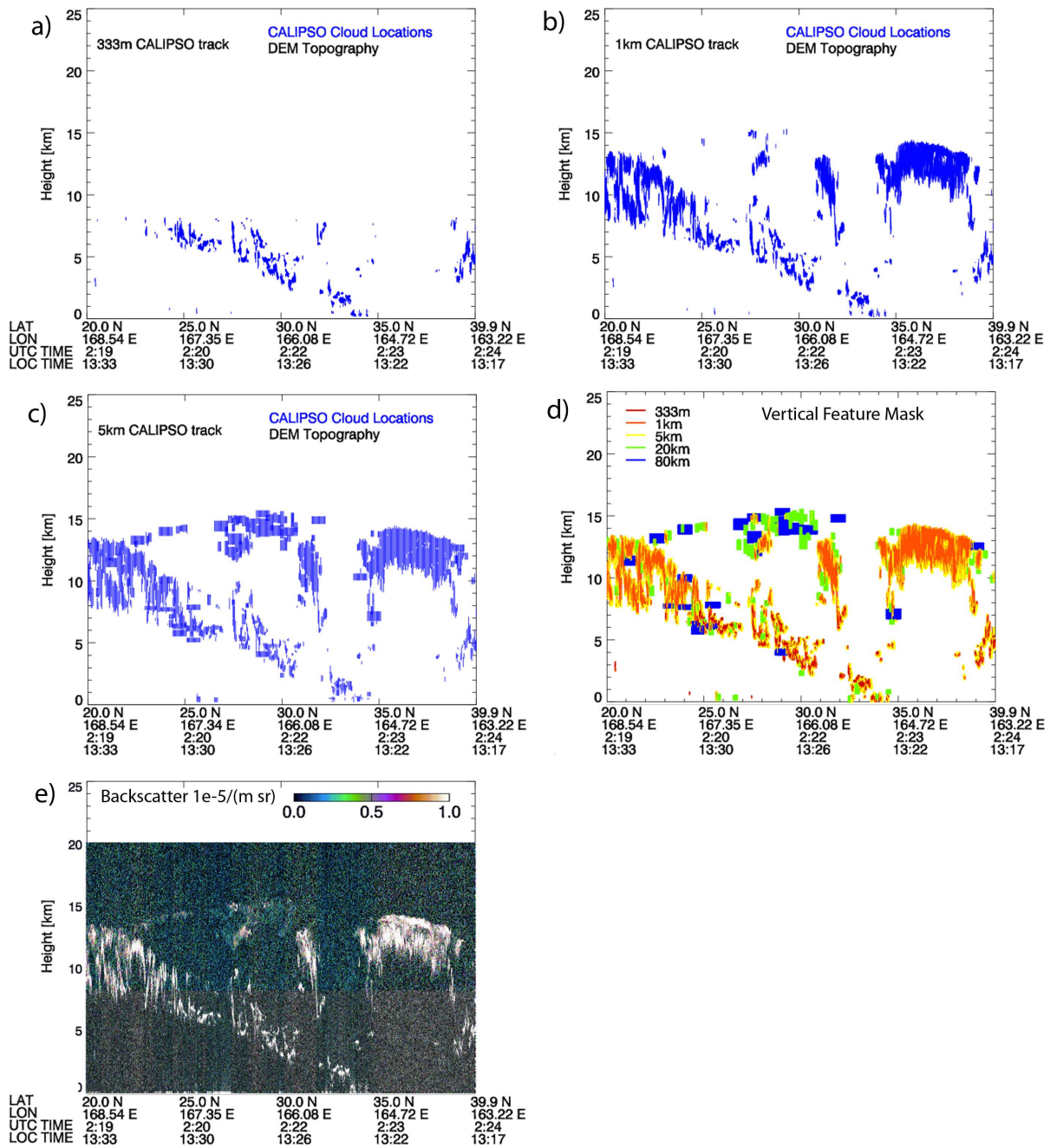


Figure 3.2: Partial CALIPSO track from July 1st 2008. Panels a), b) and c) show the clouds reported in the 333 m, 1 km, and 5 km cloud layer products respectively. Panel d) shows all clouds reported in the vertical feature mask, colour coded by the amount of averaging necessary for detection. Panel e) shows the raw backscatter from the same section of the track, up to 20km.

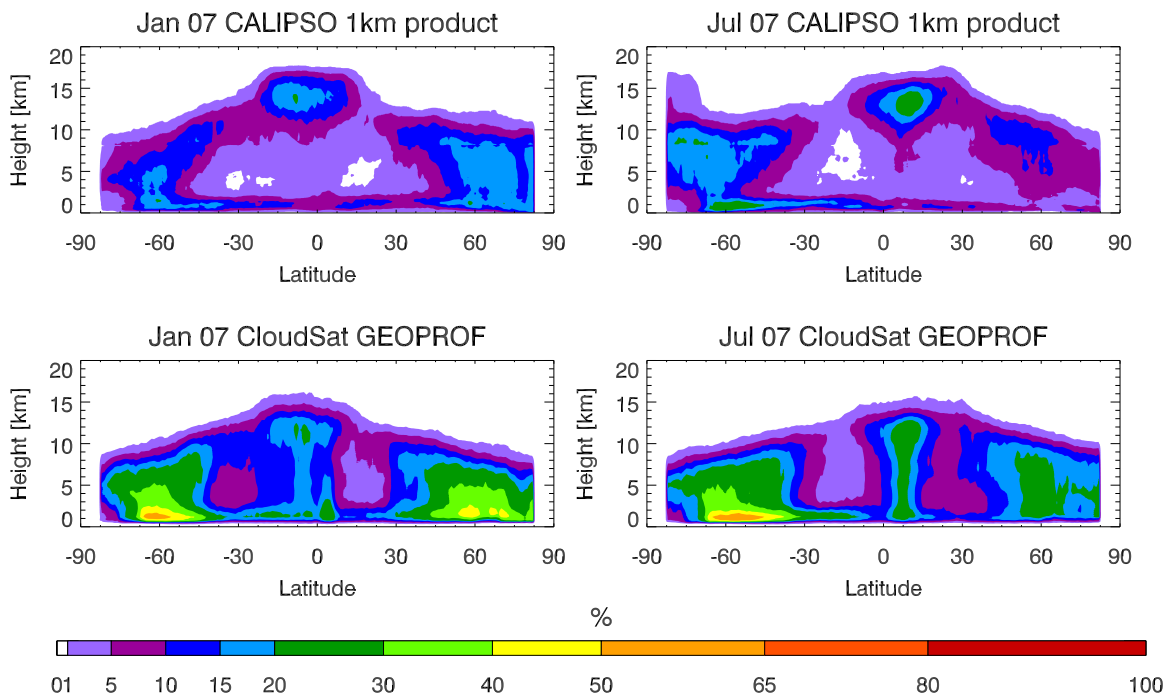


Figure 3.3: Zonal cross-section of frequency of occurrence of hydrometeors from (top row) the CALIPSO 1km product, (bottom row) the CloudSat “GEOPROF” product for January (left panels) and July 2007 (right panels).

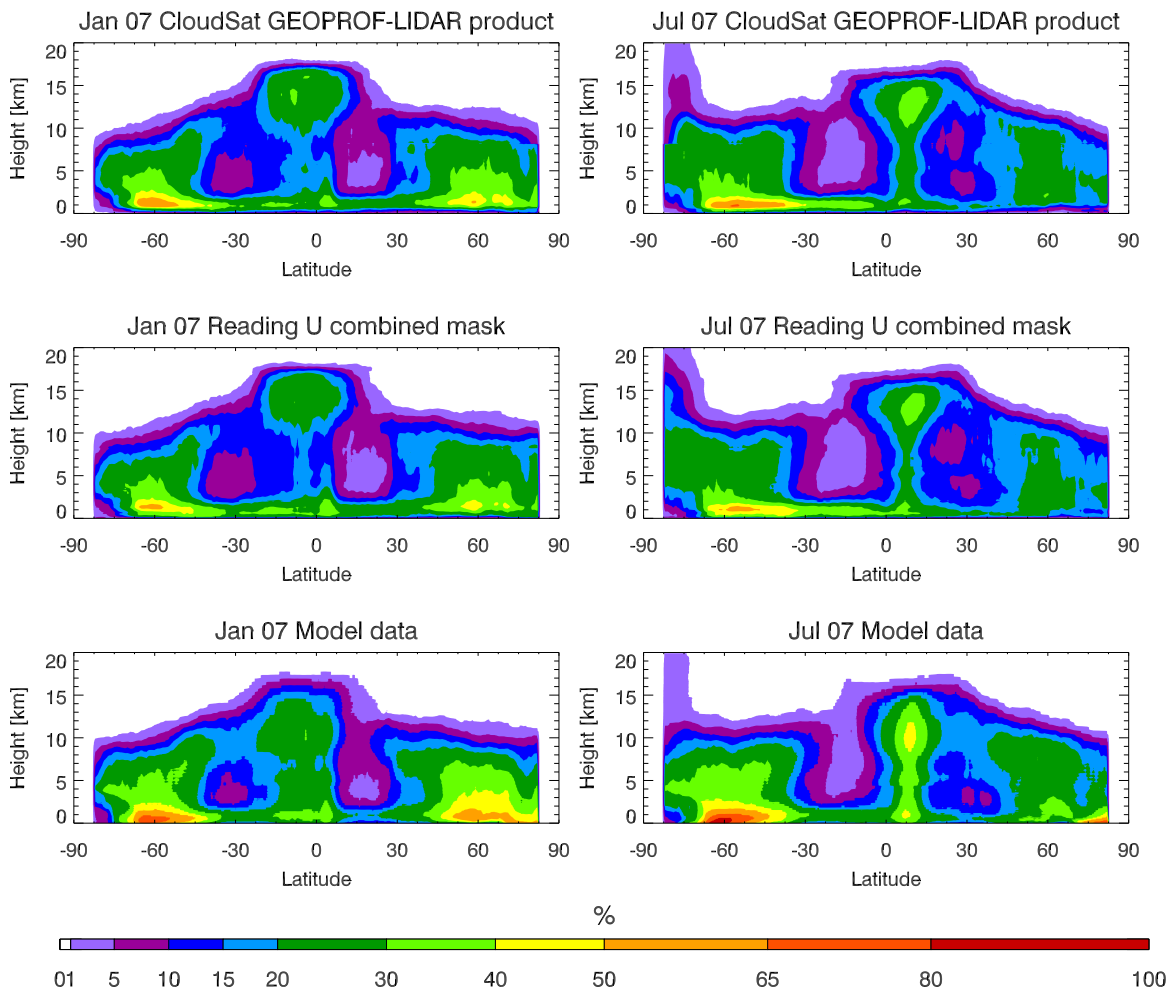


Figure 3.4: Zonal cross-section of frequency of occurrence of hydrometeors from (top row) the combined CloudSat and CALIPSO “GEOPROF-LIDAR” product, (middle row) the combined CloudSat and CALIPSO product from (Delanoë and Hogan, 2009), (bottom row) the IFS model cloud and precipitation derived from through the lidar and radar forward operators.

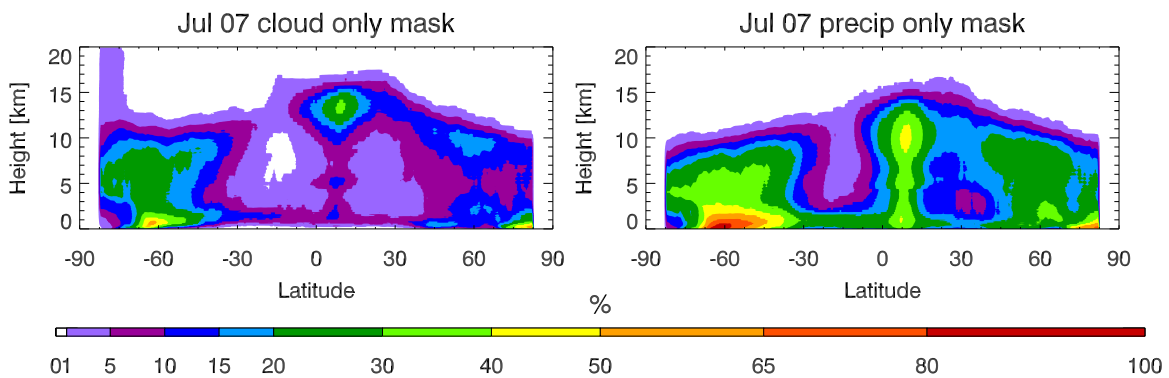


Figure 3.5: Zonal cross-section of frequency of occurrence of (a) liquid water and ice cloud and (b) rain and snow precipitation from the IFS model.

### 3.3 Evaluation of forward-modelled radar reflectivity using CloudSat

The approach taken here (as in [Bodas-Salcedo \*et al.\*, 2008](#)) is to forward model the CloudSat radar reflectivity to directly compare the temporally and spatially matched IFS model cloud and precipitation fields with the observed variable.

#### *(a) Data*

The model data is from IFS version CY35R1 with T511 spectral truncation (40 km grid resolution). A series of 12 UTC daily 12 to 36 hour forecasts are joined together to create a longer timeseries of short-range forecast data. The extracted data along the A-Train track always has a model validity time within 1.5 hours from time of the observation. A cloud generator is used on the model data to create a series of sub-columns representing the sub-grid scale distribution of cloud condensate and precipitation elements and their vertical overlap. Twenty sub-columns were used in the cloud generator which could be considered to be on the low side, but tests with 50 columns showed no significant differences in the results. The sub-grid distribution of ice and liquid cloud used the predicted cloud fraction, whereas the stratiform and convective precipitation were treated differently (as there is currently no prognostic sub-grid fraction for precipitation). The stratiform rain and snow were distributed with the same assumptions as in the model: the initial precipitation fraction is equal to the cloud fraction in the generation layer and maximum-random overlap is assumed with lower layers. The convective precipitation is generated from the convective cores in the convection parametrization and the convective rain and snow sub-grid fraction should therefore represent the fractional area of these cores. This is a parameter that is not defined in the model, so a representative fixed value of 0.05 (5%) is used.

The ZmVar radar reflectivity forward model described in WP1100 is then applied to each sub-column of each grid-point to generate a set of reflectivity profiles representative of the observed CloudSat reflectivity profiles at the native resolution.

#### *(b) Example cross sections of radar reflectivity*

In order to illustrate the comparison of the model radar reflectivity profiles with CloudSat, [Figures 3.6 and 3.7](#) show two examples of observed and modelled radar reflectivity along-track cross-sections across a mid-latitude front and a region of tropical convection respectively. [Figure 3.6](#) highlights the ability of the model short range forecast to produce structures and reflectivities that are close to those observed. The main difference is the relative smoothness of the model field compared to the larger variability seen in the observed cross-section. [Figure 3.7](#) shows a similar cross-section but for a region of the tropics with both deep and shallow convection as well as cirrus anvils. Again, the model has a reasonable representation of the locations, structures and reflectivities of the observations, but the deep convection is over-done in this particular case and the smoother structures of the model are evident. In both cases, the reflectivities in the shallow low-level cloud are systematically higher than observed which is due to the model cloud generating drizzle or rain (with high reflectivities) when the observations are showing that the low-level signal is mainly cloud (without precipitation). These are only two small data samples that are not necessarily representative, but are useful to illustrate the data comparison and a statistical analysis of monthly data follows.

#### *(c) Results from regional comparisons*

A statistical comparison of the model radar reflectivity field is performed for the months of January and July 2007. [Figures 3.8 and 3.9](#) show the frequency of occurrence of a range of radar reflectivities and a range of heights over ocean points only for five latitude bands (northern hemisphere high-latitudes, NH mid-latitudes, tropics, southern hemisphere mid-latitudes and SH high latitudes) for the two months repre-

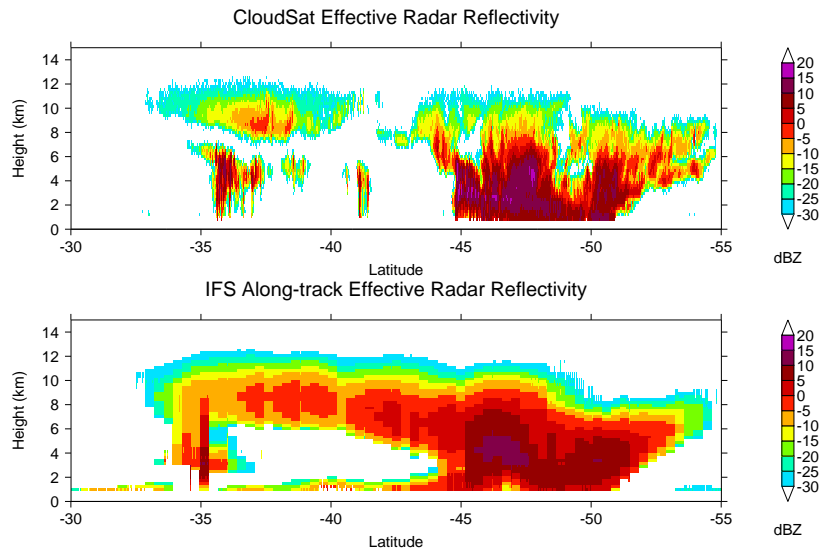


Figure 3.6: Example cross-section of radar reflectivity from CloudSat (upper panel) and from the IFS model (lower panel) for a mid-latitude front.

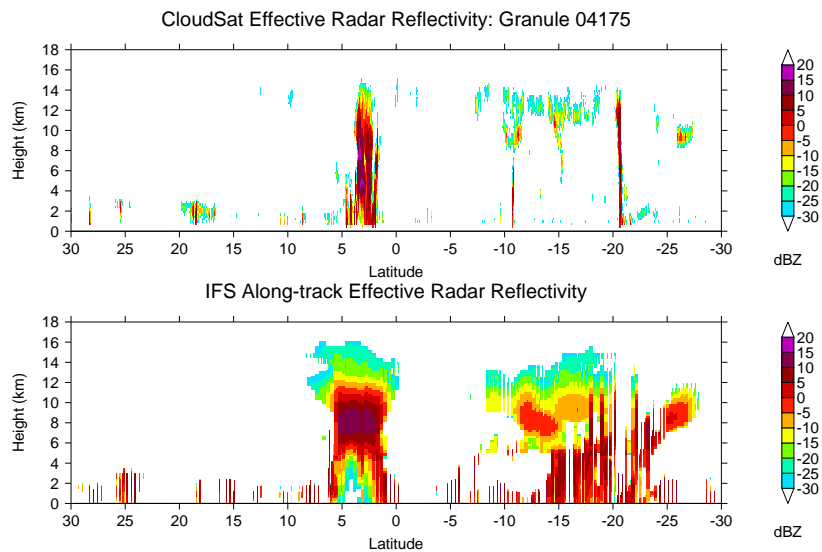


Figure 3.7: Example cross-section of radar reflectivity from CloudSat (upper panel) and from the IFS model (lower panel) for tropical convection.

sentative of northern hemisphere winter (Jan) and summer (Jul). There are differences between regions and seasons in the observations and the model is able to capture these main differences and represent a significant proportion of the variability of reflectivity with height. There are also a number of differences between the model and observations:

- A general overestimation of the frequency of hydrometer occurrence, although this depends on region and altitude. This may be partly due to an overestimation of cloud fraction, smoothness of the dynamical forcing due to the limited resolution of the model, or overestimation of the precipitation fraction.

The formulation of the diagnostic precipitation fraction does have an impact as it is sensitive to the assumed precipitation overlap and the assumed precipitation fraction for convection. Increasing the convective cloud cover from 5% leads to a greater frequency of hydrometeor occurrence in the model.

- A relative lack of occurrence of lower reflectivity values at mid-levels (2-8 km), which generally relates to ice water cloud. There is either not enough variability of ice water content in the model, or the model produces small amounts of precipitating snow too readily which overestimates the particle sizes and hence reflectivities.
- A lack of high reflectivity values at mid-levels. For example, CloudSat reflectivities in Fig. 3.8(c) occur up to 15 dBZ between 4 and 8 km altitude, whereas the model is limited to 5-10 dBZ. This relates to the precipitating snow in the model, particularly convective, which either does not reach the large water contents that are present in reality, or has mis-represented the particle characteristics used in the radar reflectivity forward model. These high values are sensitive to the particular assumptions of ice particle size, shape and density.
- At low levels (1-2 km altitude), the observations have a wide spread of reflectivity values representing cloud (-30 to -20 dBZ), drizzling cloud (-15 to 0 dBZ) and heavier rain (0 to 10 dBZ) whereas the model is dominated by the higher reflectivity rain mode, particularly pronounced in the tropics (Figs. 3.8c and 3.9c). The over-occurrence of precipitating shallow convection can also be seen in the example cross section in Fig. 3.7.
- A large overestimation of low level cloud in northern hemisphere high latitudes in the summer month (Fig. 3.9a).

In addition to the zonal breakdown, results from a limited number of regional areas dominated by a particular low-cloud regime (stratocumulus and trade cumulus) are shown in Figure 3.10. The three main stratocumulus regions show broadly similar results in the south-east Atlantic, south-east Pacific and north-east Pacific off the California coast, with very good agreement for the overall frequency of occurrence of hydrometeors, but again the model has a much more dominant rain mode than the observations. The observations in the trade cumulus regime (Fig. 3.10d) show a more frequent occurrence of deeper high reflectivity (raining) cloud as expected, which the model also represents, but it also overestimates the frequency of occurrence of these raining clouds in the lowest few km.

#### *(d) Summary*

A preliminary evaluation of the ECMWF model derived radar reflectivity with CloudSat has provided global and regional information on vertical profiles of cloud and precipitation highlighting the positive and negative aspects of the model simulation. Over-prediction of raining versus non-raining low-level cloud is evident in the ECMWF model as well as differences in the ice phase. The low-level cloud rain over-prediction is in part related to the shallow convection scheme and microphysics in the model and is discussed further in the concluding remarks in Section 5. This evaluation using radar reflectivity highlights particular aspects of the model that may not be as evident in other observations. The representation of precipitating rain and snow is particularly evident from this comparison as they tend to dominate the radar reflectivity signal. There needs to be some caution in interpreting the results due to the sensitivity of the reflectivity to the particular microphysical assumptions in the forward model and the assumptions of sub-grid cloud and precipitation fractions. In order to provide further confidence, it is important to evaluate the model with a wide range of different observations and methodologies. The following section describes an “observation-to-model” approach using a combination of CloudSat radar and CALIPSO lidar data to derive ice water content as an alternative evaluation of the model ice-phase cloud and precipitation.

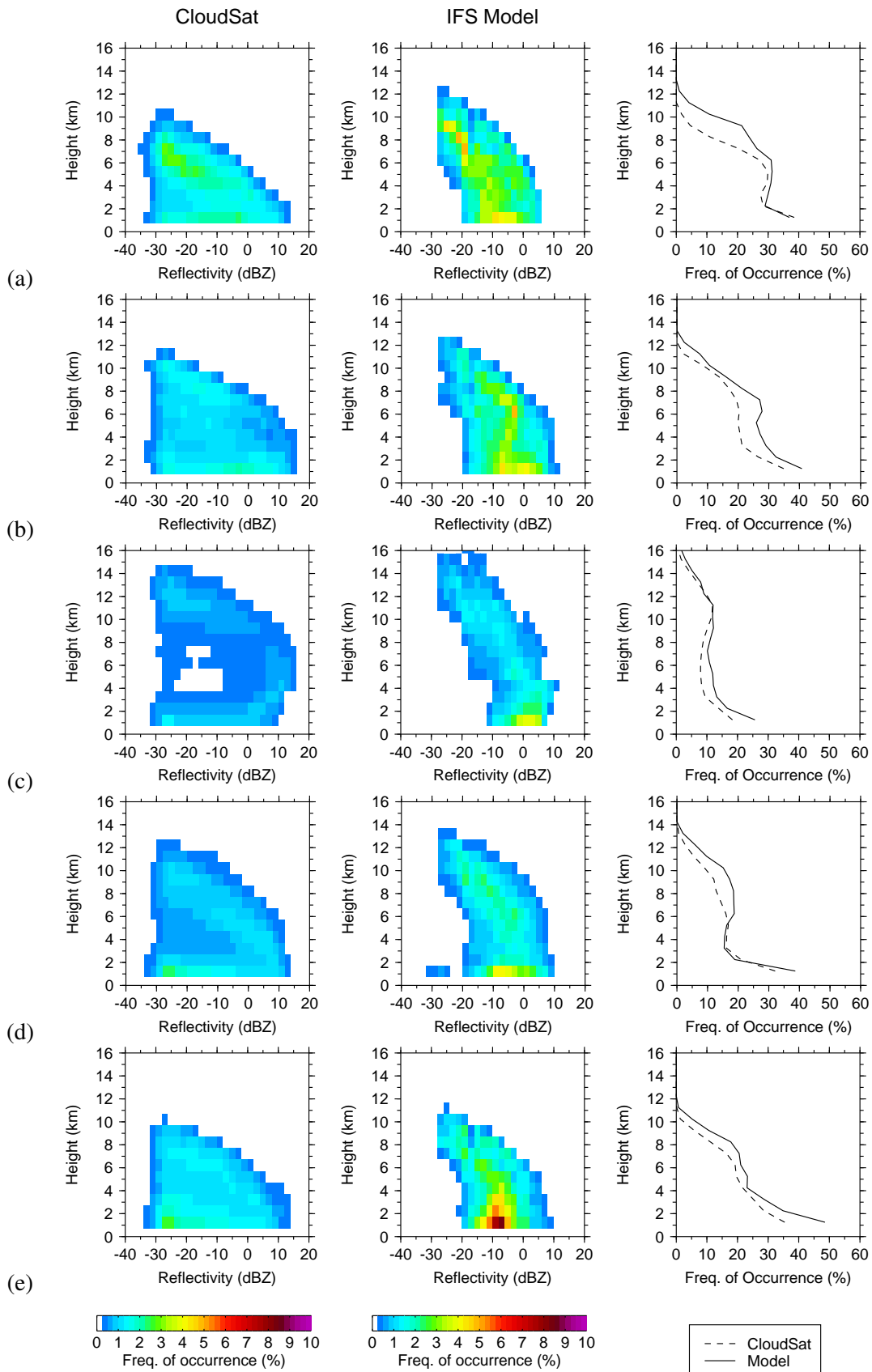


Figure 3.8: Frequency distribution of radar reflectivity with height for January 2007 (a) NH high-latitudes (60N-80N), (b) NH mid-latitudes (30N-60N), (c) tropics (30S-30N), (d) SH mid-latitudes (30S-60S), (e) SH high-latitudes (60S-80S).

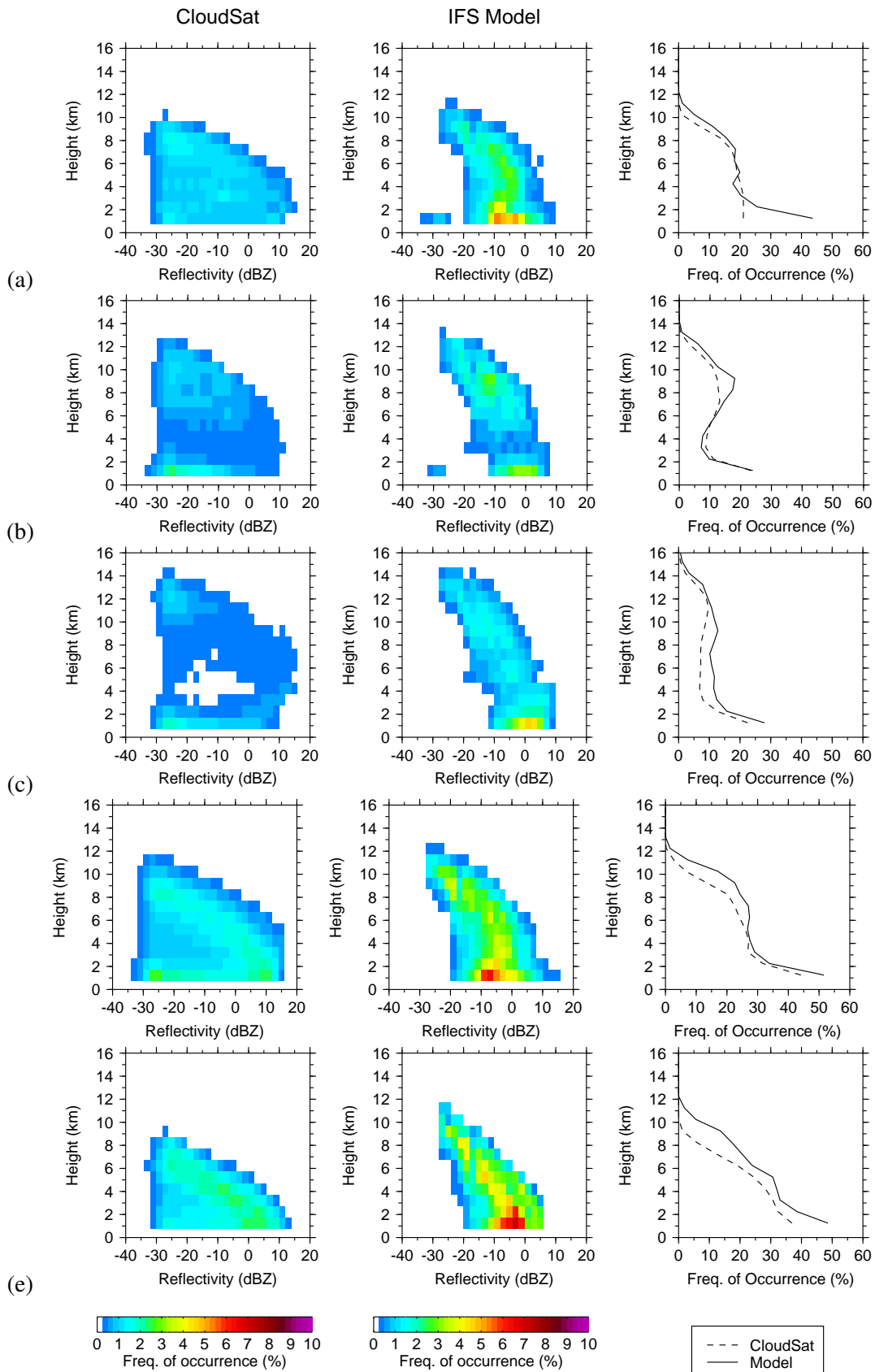


Figure 3.9: Frequency distribution of radar reflectivity with height for July 2007 (a) NH high-latitudes (60N-80N), (b) NH mid-latitudes (30N-60N), (c) tropics (30S-30N), (d) SH mid-latitudes (30S-60S), (e) SH high-latitudes (60S-80S).

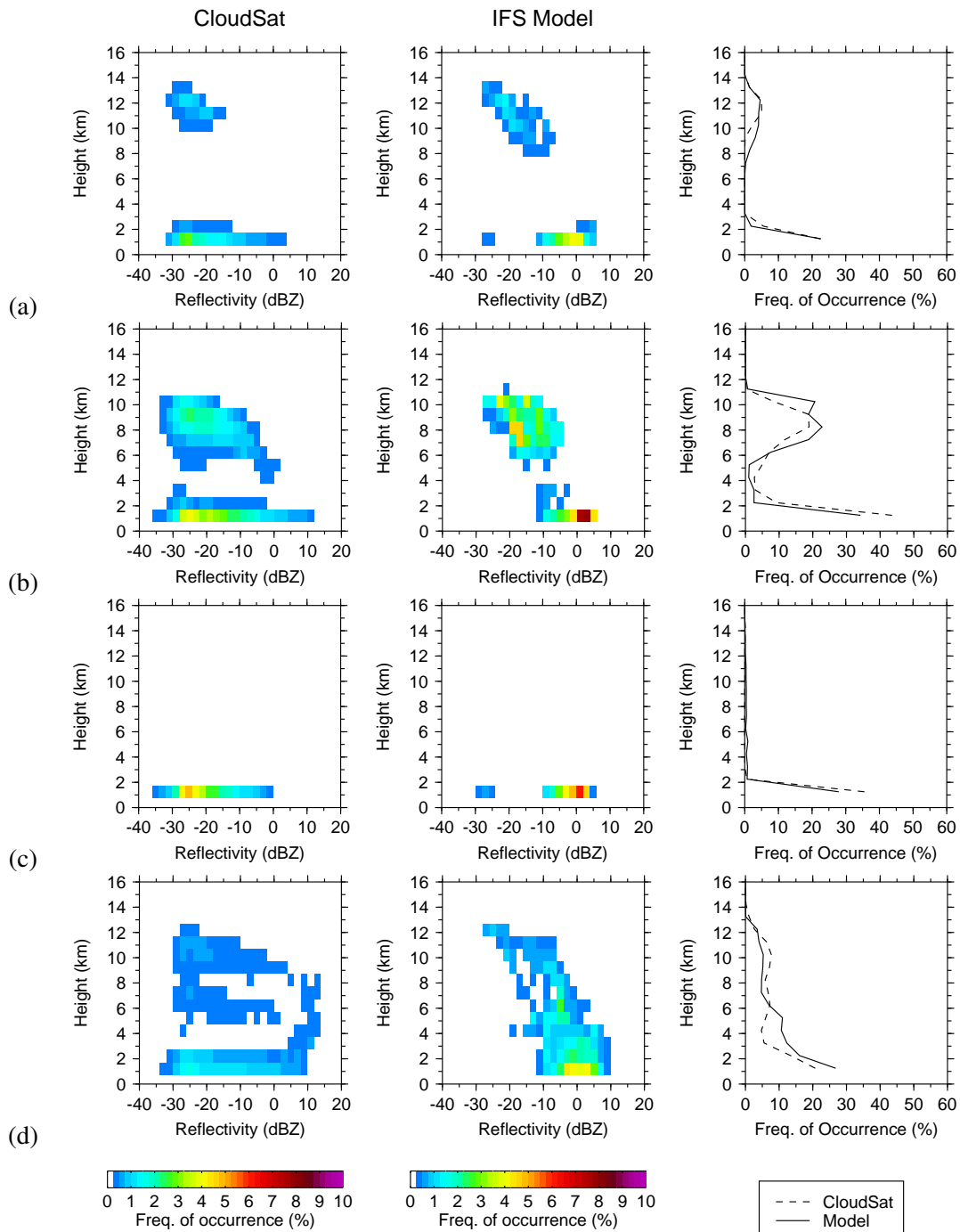


Figure 3.10: Frequency distribution of radar reflectivity with height for July 2007 (a) South-east Atlantic oceanic stratocumulus region (20W-20E, 30S-Equator), (b) South-east Pacific oceanic stratocumulus region (100W-70W, 40S-10S), (c) North-east Pacific oceanic stratocumulus region (California coast) (140W-110W, 15N-45N), and (d) west Atlantic oceanic trade cumulus (70W-30W, 15S-30N).

### 3.4 Evaluation of ice water content using a combined radar/lidar technique

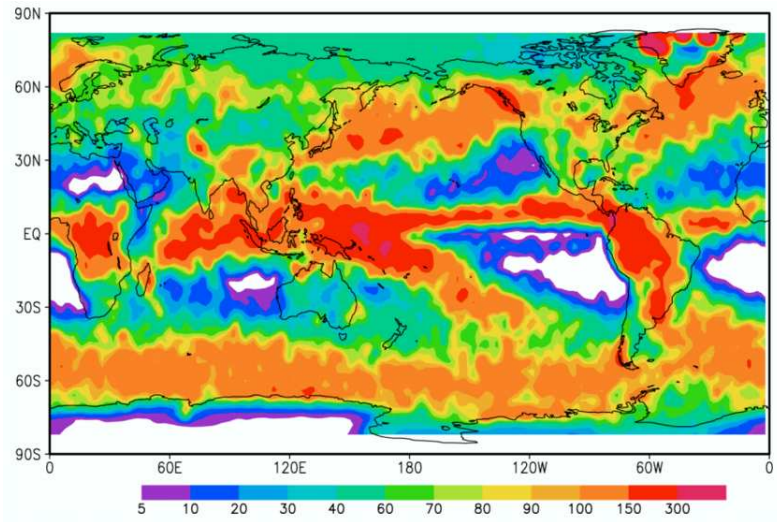
The IFS model has ice water content (IWC) as one of the main prognostic cloud variables (part of the condensate variable as described in Section 2) and is an important quantity in terms of the impact on the hydrological cycle and radiation. Although the radar reflectivity comparison in the previous section highlighted a number of issues with the model, it is also relevant to approach the model validation from as many different angles as possible to provide information on what aspects of the parametrization need to be improved. This section describes an example of the “observation-to-model” approach, deriving a direct model-predicted quantity from a set of observations. There are different assumptions that are required in the observation retrieval process, but utilising the synergy of different instruments providing complementary information can narrow the uncertainty in the derived estimates of IWC. Both the model with the current version of the cloud scheme and the new version with additional prognostic variables are assessed.

#### (a) Data

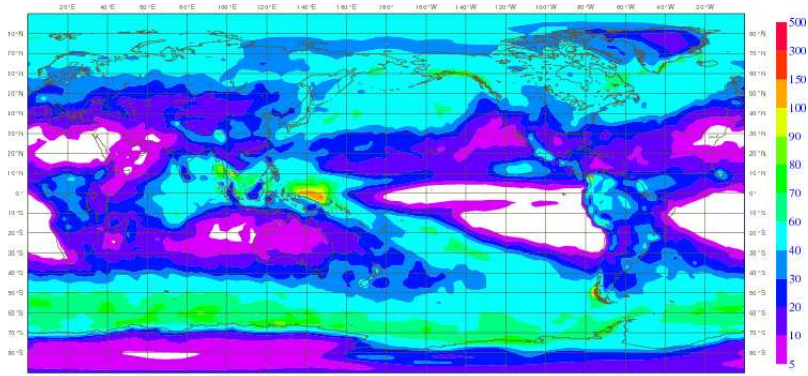
Ice water content profiles are available as part of the CloudSat Radar-Only cloud Water Content Product (2B-CWC-RO) which contains retrieved estimates of cloud liquid and ice water content, effective radius and related quantities for each radar profile. This is a single-instrument product and there is benefit from a multi-instrument approach to deriving IWC by exploiting synergy of the different instruments to give improved estimates of particles size and optical properties. [Delanoë and Hogan \(2008\)](#) proposed a variational method to use synergy of radar, lidar and infrared radiometer to retrieve ice cloud water content from ground-based instruments. The approach has the benefit of a seamless retrieval of cloud properties between regions of cloud detected by both radar and lidar, and regions detected by just one instrument. [Delanoë and Hogan \(2009\)](#) describe the application of the algorithm to space-borne radar, lidar and radiometer instruments onboard the A-Train satellites. The zonal average of the cloud feature mask derived from this retrieval was shown in Section 3.2. In this section the IFS model with the two versions of the cloud scheme described in Section 2 are compared with IWC derived from the CloudSat (2B-CWC-RO) product and the [Delanoë and Hogan \(2009\)](#) retrieval applied to CloudSat and CALIPSO data.

#### (b) Global ice water path

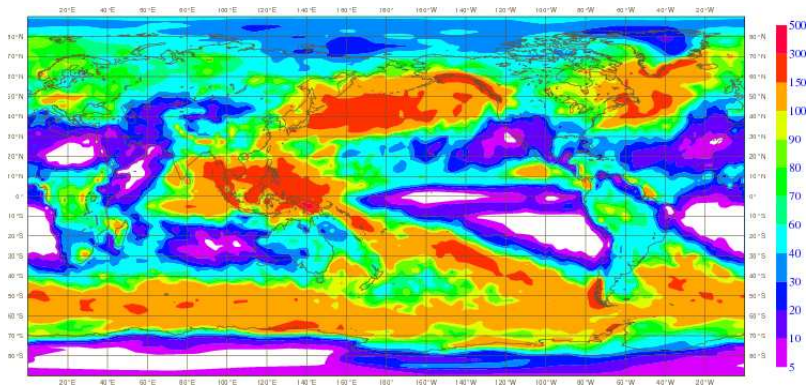
Figure 3.11(a) shows the global annual mean ice water path (IWP) (total column integrated ice water content) derived from the CloudSat GEOPROF product ([Waliser et al., 2009](#)) showing particularly high values (over  $150 \text{ g m}^{-2}$ ) in the region of the tropical warm pool, along the ITCZ and over the tropical South American and African continents. The mid-latitude oceanic storm tracks in both hemispheres also show high values of IWP (over  $100 \text{ g m}^{-2}$ ). Minima in the IWP field occur in the sub-tropical stratocumulus regions in the eastern part of the ocean basins and over the Sahara in Africa. The second panel in Fig. 3.11 shows the IWP derived from the single prognostic ice water content variable in the current IFS model, clearly showing the significance of the precipitating snow field contribution to the total IWP. Although the snow IWP could be derived from the diagnostic precipitating snow variable in the model, it does not interact with the radiation scheme. The IWP from the new version of the cloud scheme with radiatively active prognostic ice and snow variables is shown in Fig. 3.11(c). Including both the ice cloud and precipitating snow variables brings the model much closer to the observed IWP. The overall pattern is well represented by the model, although there are differences in the magnitude of the IWP with an underestimate in the tropics and an overestimate in the northern hemisphere storm tracks. Given the wide range of IWP from different global models that contributed to the IPCC 4th Assessment Report shown in [Waliser et al. \(2009\)](#), the ECMWF model with the new cloud scheme is remarkably consistent with the CloudSat estimate. There is of course some level of uncertainty in the CloudSat IWP product, but this is difficult to quantify at this stage.



(a)



(b)



(c)

Figure 3.11: Annual mean global ice water path ( $g\ m^{-2}$ ), (a) derived from CloudSat observations from Waliser et al. (2008), (b) column integrated ice water content variable from the current IFS model, (c) column integrated ice + snow water content variables from the IFS model with the new version of the cloud scheme. Note the non-linear scale.

*(c) Ice water content profiles*

The rest of this section focuses on the ice water content (IWC) products produced from the method of Delanoë and Hogan (2009) using combined radar, lidar and infrared radiometer data. A comparison of the derived IWC with the current model version and with the new cloud scheme is performed for 3 weeks of data in July 2006. As before, the model data is extracted from 3-hourly instantaneous data for the 12-36 hour forecasts along the CloudSat track to create a continuous timeseries of model profiles always within 1.5 hours of the CloudSat overpass time. An example of an along-track cross-section comparing the IWC profiles from the observation derived dataset and the two versions of the model is shown in Figure 3.12. Similar to the previous figure, only IWC from the ice prognostic variable is shown in the middle panel from the current version of the model, whereas the IWC from the new version in the lower panel is from the combined ice and snow prognostic variables. The much higher values of IWC and the continuing increase in IWC as the melting layer is approached is more realistic in comparison with the observations (top panel). It is not only the fact that precipitating snow is included in the new version, but also that the ice variable is no longer a diagnostic function of temperature. In the current model, the IWC fraction has to decrease nearer to the melting level, giving a maximum that is at much higher altitude (colder temperature) than in reality where the maxima in deep precipitating systems is often just above the melting layer.

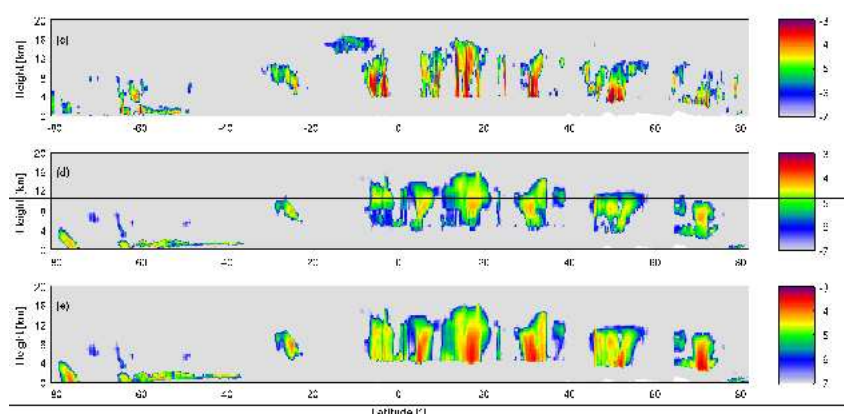


Figure 3.12: Example cross-section of ice water content ( $\text{kg m}^{-2}$ ) in July 2006 for (top panel) derived CloudSat/CALIPSO IWC using the Delanoë and Hogan (2009) technique, (middle panel) from the IFS model with one prognostic ice variable and (lower panel) from the IFS model with both ice and snow prognostic variables in the new scheme.

A statistical comparison of the occurrence of different ice water contents at different temperatures is presented as 2D PDFs in Fig. 3.13. Each panel shows the frequency of occurrence as a function of IWC and temperature (from 0 to  $-80\text{C}$ ) for the observation derived IWC product and the two versions of the model for different geographical regions (in order from top to bottom; global, northern hemisphere, northern mid-latitudes, tropics, southern mid-latitudes, southern hemisphere). The top row shows the global PDF and highlights many of the main similarities and differences between the observations and the two versions of the model. The main point to note is how well the model captures the variability in IWC values across the temperature range, an aspect that not all models can represent adequately. The basic shape of the PDF is similar, with a wide variation in IWC values just above the melting layer, and then a band of decreasing IWCs with decreasing temperature (increasing altitude). The primary difference between the two models is in the  $-20\text{C}$  to  $0\text{C}$  range where the precipitating snow and additional degree of freedom for the prognostic ice variable dramatically increase the high IWCs present. In this respect, the new version of the cloud scheme is much closer to the observed distribution. However, the model still underestimates the spread of IWCs at these warmer temperatures and also underestimates the very high IWC in this temperature range. Both models underestimate the frequency of occurrence of the lower IWC values at very cold temperatures ( $-70\text{C}$  to  $-80\text{C}$ ) (discussed below)

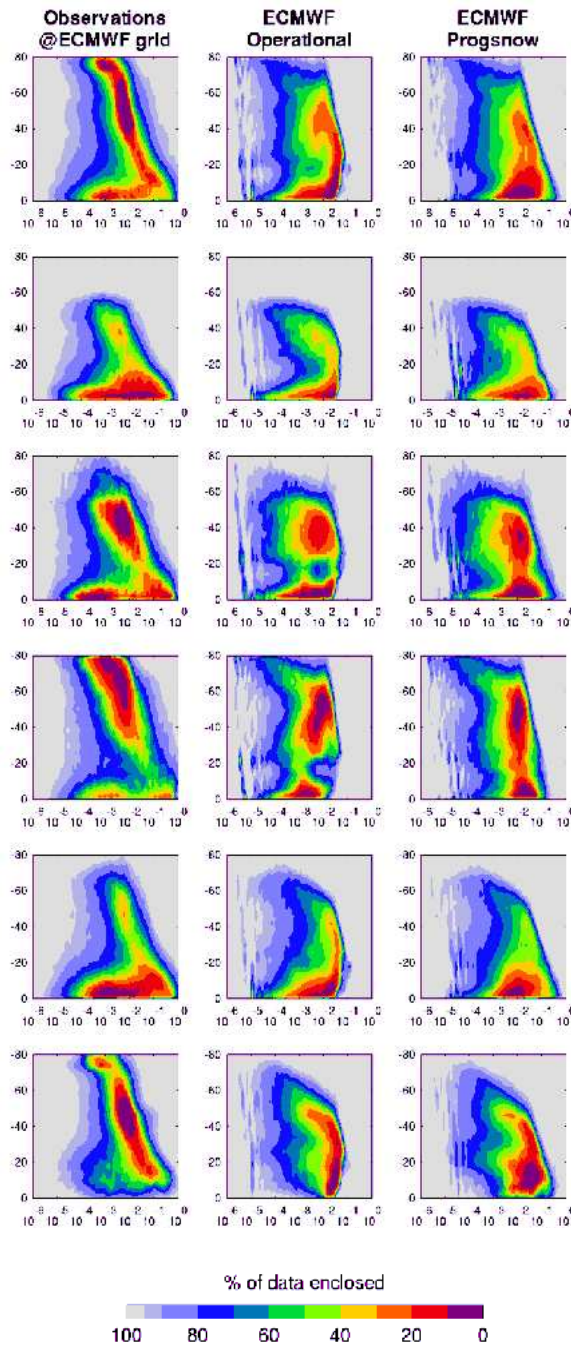


Figure 3.13: PDFs of ice water content vs. temperature for different regions (global, NH high latitudes, NH mid-latitudes, tropics, SH mid-latitudes, SH high latitudes) for the observations (left), current ECMWF model with one ice prognostic variable (centre) and model with the new cloud scheme with both ice and snow prognostics and independent liquid water. The contours show the percentage of the data that is enclosed within each contour to highlight the spatial patterns in the data.

Breaking the statistics down into different regions, again shows the success of the model in describing the overall shape of the PDFs which vary markedly with latitudinal band due to the different meteorological regimes. The same comments as above apply to the different region, but one other point to note is the under-prediction of the frequency of occurrence of low IWC cloud at very cold temperatures (colder than -60C) which relates to the deep convection penetration to very high altitudes in the tropics and stratospheric

cloud in the Southern Hemisphere. There may still be some issues with the observations and retrieval process, which are under investigation, including sensitivity of the retrieval to microphysical assumptions, identification of polar stratospheric clouds and the possibility of specular reflection affecting the nadir-pointing lidar return in the July 2006 data with the potential for inaccurate IWC estimates, particularly at very cold temperatures.

Figure 3.14 shows the global average vertical profiles (as a function of temperature) for the number of grid boxes containing ice cloud (i.e. frequency of occurrence), average grid-box cloud fraction and grid-box average IWC. The underestimation of the frequency of occurrence of ice cloud at very cold temperatures seen in the previous figure is clearly evident. Between  $-50$  and  $-20$  C, both models overestimate the occurrence, but only the new version of the model significantly overestimates the occurrence at temperatures warmer than  $-20$  C. However, the good agreement between the current model and the observations at these warmer temperatures is probably for the wrong reasons, as precipitating snow is present in the observations and missing from the data from the model used here. It is likely therefore that this overestimate relates to a more general model problem and is consistent with the analysis of the radar reflectivity comparison in Section 3.3. The cloud fraction profile in Fig. 3.14(b) shows a similar pattern with the both versions of the model overestimating cloud fraction at sub-zero temperatures and the new version more so at temperatures warmer than  $-40$  C. However, Fig. 3.14(c) shows both models underestimate the grid-box average IWC, but the new version is much more consistent with the observed profile. If the IWC and the cloud fractions are lower than observed, then the in-cloud IWC seen by the radiation will also be low, perhaps compensating the over-occurrence of cloud in the model.

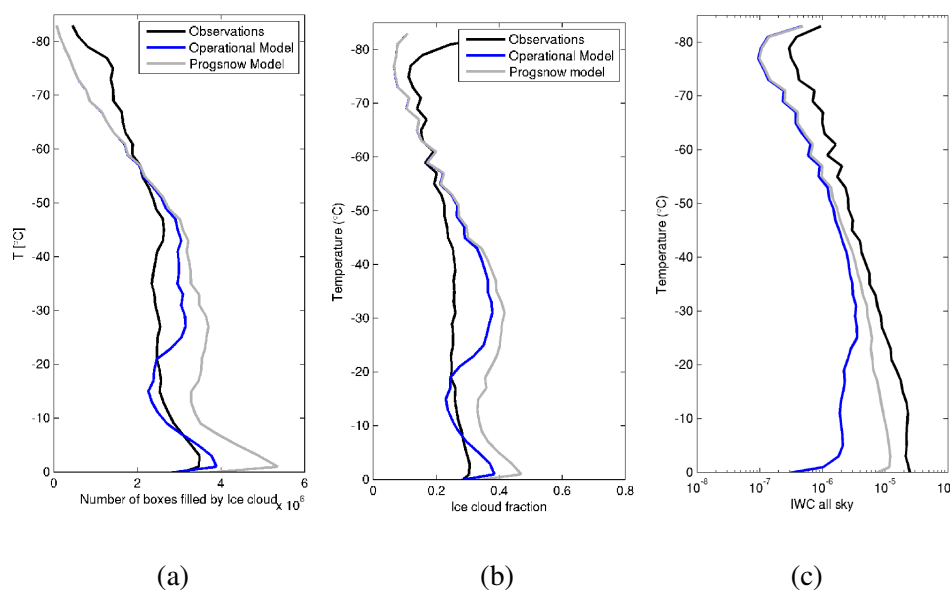


Figure 3.14: Global average vertical profiles for the IWC observations, current model (“operational model”) and the new prognostic cloud scheme (“progsnow”), (a) number of grid boxes containing ice cloud (frequency of occurrence), (b) average grid-box cloud fraction and (c) average IWC.

### 3.5 Evaluation of trade cumulus in the ECMWF model using CALIPSO observations

Over the past few years, the boundary layer parametrization in the IFS has been extended to include boundary layer clouds (stratocumulus) under certain conditions (Tompkins *et al.*, 2004; Köhler, 2005) and now a further extension is being tested that will incorporate aspects of the shallow convection parametrization in the boundary layer scheme (Neggers, 2009; Neggers *et al.*, 2009). These are some of the motivating factors

for the evaluation of trade cumulus clouds over several cycles of the IFS. Coincidentally, the trade cumulus regime lends itself well to an evaluation with CALIPSO observations: trade cumulus clouds are ubiquitous in the subtropical oceans, where optically thick high clouds, which might obscure the view of clouds below, are rather uncommon.

#### (a) Data

The CALIPSO 1km cloud layer product is used here to create a cloud mask. The model is run at T399L91 resolution (approx. 50km grid resolution, 91 levels), initialized every other day. Three-hourly output from forecast hours 24-72 is stitched together for a continuous record. Model data are extracted along the satellite track, matching the overpass time with the nearest forecast step, and only the “curtain” of model columns along this track is compared to the observations. In total, six months are analyzed (January 2007, 2008, 2009 and July 2006, 2007, 2008). Since the results are very similar for all six months, figures are only shown for one month here.

#### (b) Strategy

This evaluation aims to answer the question whether the model has the right amount of trade cumulus clouds in the right area, and whether these clouds have characteristics comparable to those observed. In order to address these questions, we chose an obs-to-model approach: the observed clouds from the CALIPSO 1 km layer product are recast onto the model grid to produce a cloud mask. Typically, fifty 1 km lidar observations fall into a model grid box at T399 resolution. A vertically resolved along-track cloud fraction can be calculated from the lidar observations falling into each model column along the satellite path. A few simple criteria are used to identify each grid column containing trade cumulus clouds:

- Only ocean points between  $30^{\circ}N$  and  $30^{\circ}S$  are considered.
- The column-average cloud top height must not exceed 4 km.
- The cloud fraction must not exceed 50%.

One advantage of keeping the selection criteria simple is that no *a-priori* information derived from the model is needed to identify samples in the observations, and the sample selection between model and observations remains truly independent.

A similar methodology has been successfully tested for the evaluation stratocumulus cloudiness in the ECMWF model (Ahlgrimm *et al.*, 2009). The details for the calculation of the column-average cloud top height can be found in that article.

#### (c) Results

Figure 3.15 shows the frequency of occurrence of samples identified as ‘trade cumulus’ in the observations (upper panel) and model (lower panel) for July 2007. During the month of July, the satellite passed over roughly 96,000 ocean grid boxes falling into the 30S to 30N region. In about 45% of those cases, the lidar observed clouds that were classified as trade cumulus, while in the model 65% of those grid points contain trade cumulus. This is evident in the darker shading (higher frequency of occurrence) seen in the lower panel of Fig. 3.15. However, the areas where those samples were identified are quite similar: most of the

ocean basins, excepting the stratocumulus regions, frequently contain trade cumulus clouds. The frequency is also reduced in areas where deep convection is typical. Here, the lidar's signal is attenuated higher up, and boundary layer clouds cannot be observed. To account for this shielding effect, a lidar simulator is run in the model. Each model column is divided into approximately 50 sub-columns using the generalized overlap assumption to determine each subcolumn's clear and cloudy layers. If the simulated backscatter is fully attenuated in more than half the subcolumns, then any clouds below are assumed to be obscured.

The maps in Fig. 3.15 seem to suggest that the model has too much trade cumulus cloudiness. However, the frequency of occurrence is only one aspect of the cloud amount. Figure 3.16 shows distributions of observed (top) and modelled (middle & bottom) distributions of cloud amount when present (AWP) for the trade cumulus samples. The distribution shows that the majority of the additional 20% trade cumulus samples in the model have small cloud fractions.

The panels in the right columns of Fig. 3.16 show the distributions of column-average cloud top height. In the observations (top), the peak of the distribution lies around 800 m, with a skewed tail towards higher cloud tops: Clouds with low tops are observed most frequently, while deeper clouds are found less often. In the model (middle panel), the peak of the distribution lies around 1.5 km. The tops are more normally distributed, and higher cloud tops are observed more frequently.

Figure 3.16, bottom row, shows the cloud fraction and top height distributions for the IFS with the new dual mass flux parametrization. Around 70% of ocean samples contain trade cumulus clouds, even more than in the previous model version. However, the cloud amount when present has shifted further towards lower values - many of the additional samples have less than 10% cloud fraction, and there are fewer samples with fractions above 30%. The cloud top distribution has improved markedly. The peak of the cloud top heights is now in very good agreement with observations. The number of samples with higher cloud tops remains greater than observed, though.

Since the lidar is attenuated at around optical depth 3, it cannot measure optical depth beyond this critical level. However, the frequency of full attenuation is available. In the observations, roughly 30% of the trade cumulus samples are fully attenuated, while the model has about 60% of optically thick samples. The lidar simulator used to calculate the level of full attenuation in the model does introduce some uncertainty, but it seems clear that the model's clouds are optically thicker than those observed by CALIPSO, in both versions of the IFS.

#### *(d) Summary*

In summary, the evaluation with CALIPSO observations shows that the trade cumulus cloud tops are too high in the control version of the model. Introduction of the dual mass flux parametrization greatly improves the cloud top height distribution. The evaluation also highlights that the model compensates lower-than-observed cloud AWP with an increased frequency of occurrence. However, there is an as-yet unknown uncertainty associated with the cloud fraction estimate from CALIPSO due to the sampling error. This problem is discussed in some detail in section 4. Also, the cloud amount estimates in this evaluation only take into account trade cumulus samples, but do not include errors in other cloud regimes. For example, the apparent overestimate in trade cumulus cloud cover might be balanced by an underestimate of stratocumulus cover. While CALIPSO is immensely useful in exploring the characteristics of the trade cumulus cloud type, data from imagers, which observe larger areas and don't suffer from the sampling error, should be used in synergy to better constrain the total cloud cover evaluation.

Out of the analyzed six months only one is shown here in the figures. The percentage of detected trade cumulus samples and fully attenuated samples varies only by one or two percent between individual months, and cloud AWP and top height distributions look almost identical. The frequency of occurrence maps show

seasonal differences, which are to be expected as the areas of deep convection and stratocumulus shift with season. This suggests that a month long record is sufficient to get a representative amount of samples to describe the trade cumulus cloud type. The noisy nature of the frequency of occurrence maps, and the small number of samples within any given model grid box show that the same is not true for sampling only one point in space. A longer record would be necessary to adequately sample the clouds at a single grid point or location.

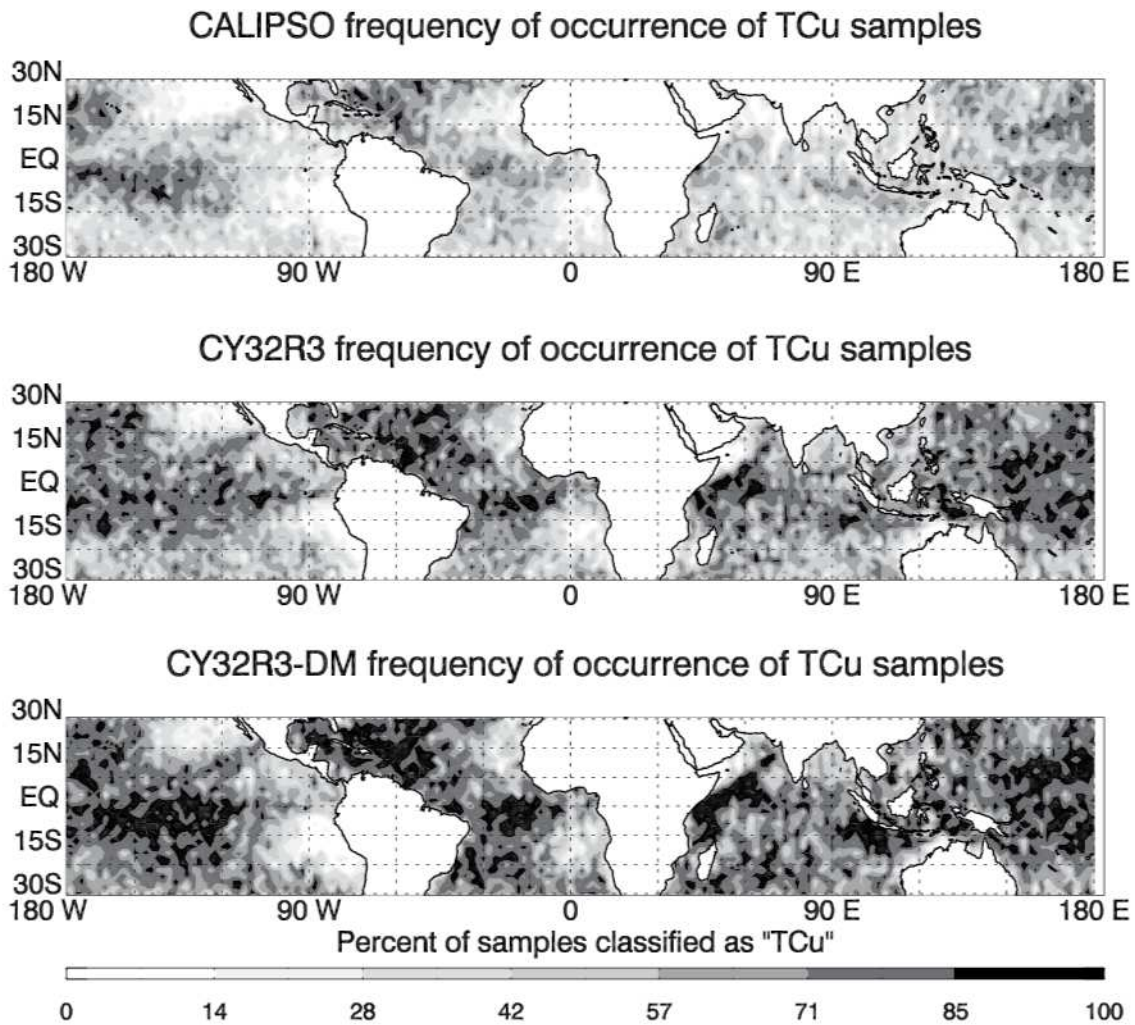


Figure 3.15: Trade cumulus sample frequency of occurrence during the month of July 2008 for CALIPSO (top), the control version of the model (middle) and the DualM run (bottom).

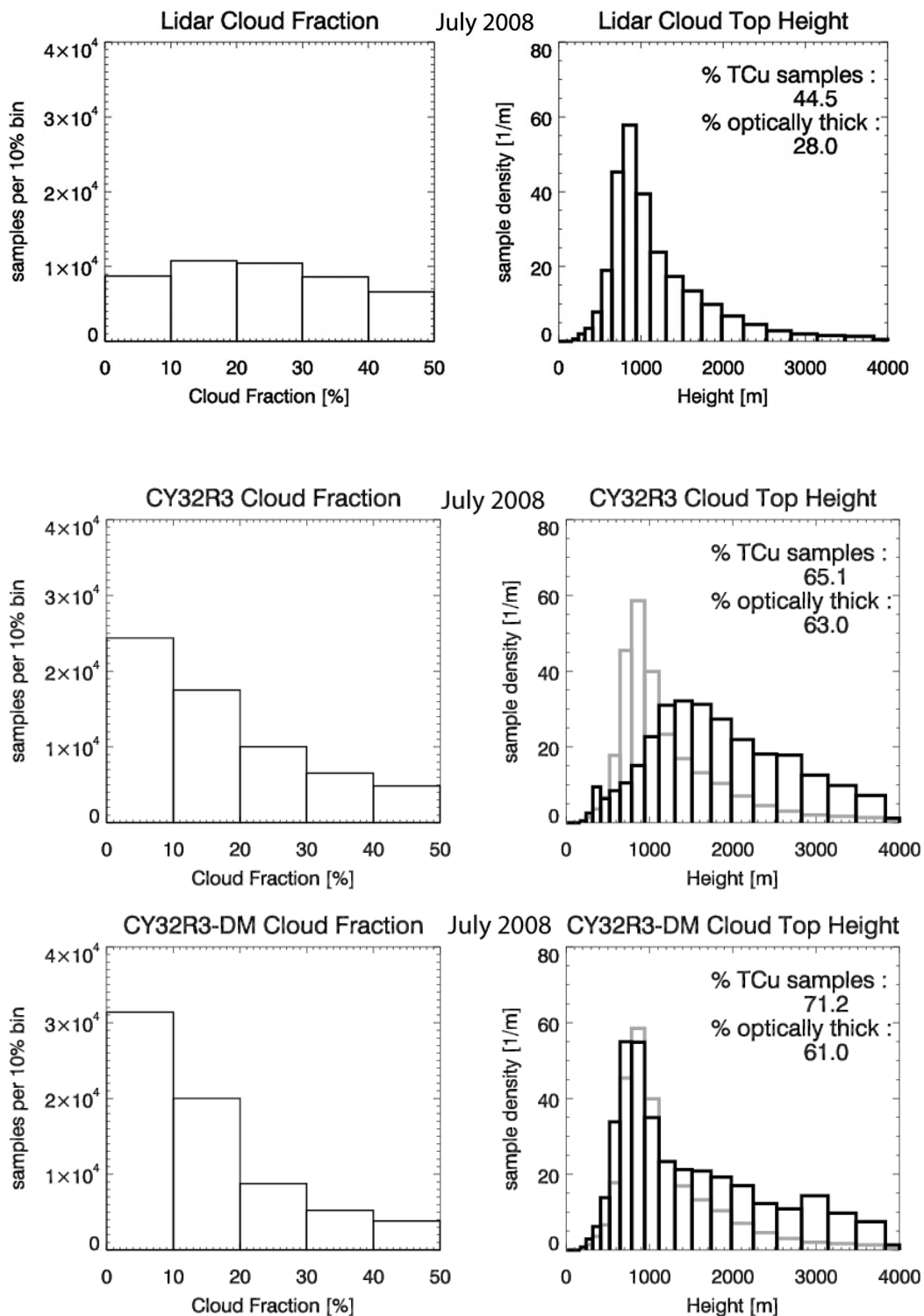


Figure 3.16: Cloud fraction (left column) and cloud top height (right column) distributions for the trade cumulus sample populations from CALIPSO (top), the control version of the model (middle) and the DualM run (bottom). The vertical axis in the cloud top height figures is a sample density, measured in detected cloud tops per width of bin, with units of  $m^{-1}$ . Shown in dark grey is the observed cloud top height distribution, for easier comparison.

### 3.6 Evaluation of precipitation from low level clouds

A key challenge for satellite-based precipitation algorithms is the improvement of detection and quantification of light precipitation (under 2 mm/hr), often associated with low-level clouds. Precipitation products derived from passive satellite instruments (e.g. AMSR-E) are not able to distinguish light rain from cloud particularly well and are also less reliable at high rain rates, whereas active radar has the potential to provide useful information across a wider range of precipitation rates. There have been a number of cloud-precipitation algorithm developments for the CloudSat radar including a method based on solely on the Path Integrated Attenuation (PIA) and an algorithm that estimates the vertical profile of precipitation (PROF) using PIA and the radar reflectivity profile,  $Z$ , with the “slope” method of Matrosov *et al.* (2006). The PIA algorithm makes use of the radar reflectivity near the surface of the earth and an estimate of path integrated attenuation (PIA) determined from the surface reflection characteristics to determine rain occurrence and intensity (Haynes *et al.*, 2009). The method depends on the well-behaved relationship between the backscatter cross section of the ocean surface and wind speed at the ocean surface, as higher wind speeds cause greater roughening of the ocean surface, resulting in increased scattering of microwave radiation away from the radar receiver and a lower resulting surface backscatter cross section.

A comparison of the model PDF of precipitation rates compared to the observation derived precipitation products for an area of the south-east Pacific ocean is shown in Fig. 3.17 (in collaboration with Prof. Graeme Stephens, Colorado State University). The frequency of occurrence in each rainrate bin is multiplied by the actual rainrate so the graph indicates the relative amounts of rainwater at the Earth’s surface that come from each rainrate. Both the observations and the model show that most of the rain water in this south-east Pacific region with significant low level cloud is occurring from the lower rainrates (< 2 mm/hr) and hence the importance of these lighter precipitation rates to the water cycle. The error characteristics of the two precipitation products are still in the process of being determined, but the difference between the two datasets gives some indication of the uncertainty. Both products should be able to detect precipitation at thresholds less than 1 mm/hr when averaged to the spatial resolution of the model grid. The results suggest the model significantly overestimates the frequency of low precipitation rates (< 1 mm/hr) in this region, which is consistent with the radar reflectivity results in Section 3.4 showing an over-occurrence of low level precipitating cloud and an under-estimate of non-precipitating cloud occurrence. For high precipitation rates (> 5 mm/hr), the model frequency agrees well with the PROF product, but underestimates the occurrence relative to the PIA product. There are still issues of uncertainty in the different precipitation retrievals and this is work in progress within the CloudSat science team.

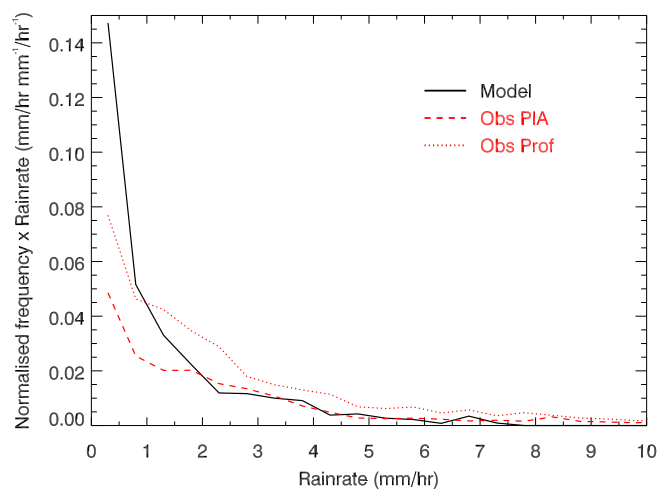


Figure 3.17: PDF of the amount of rainfall from different precipitation rates for the south-east Pacific (90W-180W, 30S-60S) from two CloudSat precipitation products (see text for a description) and the model.

## 4 Issues and limitations when comparing satellite and model data

It is clear that comparison of model data with observations is not a completely straight forward exercise. To summarise, the main issues in this context are:

1. Limits of the instruments to measure the field of interest
  - a) Instrument error (measurement accuracy)
  - b) Instrument sensitivity (e.g.: “When is a pixel considered as cloudy?”)
2. Sampling error
3. Limits of the model state to represent reality
  - a) Physical/micro-physical assumptions (e.g.: “What is the particle size of cloud particles?”)
  - b) Sub-grid assumptions in the model (“What is the 3D geometry of the subgrid cloud variables?”)

The sampling error is an important part of the representativity or representativeness error, but also errors arising from inconsistencies between the instrument sensitivity (i.e., “exactly which quantity does the instrument measure?”) and the model state limitations (“which quantity does the model represent?”) are usually referred to under the representativity issue. In general, point 3. is particularly important for model-to-observation approach which usually requires some detailed information about the 3D reality from the model state.

Many model-observation comparisons are direct verifications which assesses the agreement between model state and observations at given points in space and time (this can be done through case studies or a more statistical approach which measures the model performance with a range of statistical scores). While such verifications are of great importance for measuring the performance of an NWP system, their interpretation can be quite difficult as reasons for bad performance can be related to very different components of the NWP system. Also, most direct verification methods are very sensitive to displacement errors.

As the study presented here is more interested in the performance of individual parametrizations (particularly the cloud scheme), we have focused on a different approach and made more general comparisons of the statistics between modelled and observed data. Of course, also the interpretation of statistical differences in modelled and observed data is not necessarily easy. The hope is, however, that it indicates more clearly in which parameter regimes a model parametrisation has problems. While both data comparison types are important, regarding the limited time and resources of this project, the emphasis in the first part of the project has been on a statistical comparisons.

A major motivation for the present section is to assess at which point statistical results as they are shown in section 3.5 could be impaired by the different error types mentioned above (points 1 and 2). In principle, instrument limitations (point 1) and sampling errors (point 2) are not restricted to model-observation comparisons but can be equally important for comparisons between different observations. As the interpretation of the latter should be easier (as it is not impaired by shortcomings of the NWP system), the impact which these errors can have is illustrated with “MODIS 1D-2D” comparisons (for the sampling error) and “MODIS-CALIPSO” comparisons (for instrument sensitivities).

### 4.1 Sampling errors (1D vs 2D)

As explained above, this section focuses mainly on the impact which errors have on the statistics derived from the different data types. For estimating the sampling error involved with applications in direct verification or data assimilation we refer to the method described in Section 2 of the QuARL WP1000 report. The

question asked in this section is; “In which way does a PDF from 1D averages differ from the corresponding distribution for 2D averages”.

More specifically, we will focus on the results presented in subsection 3.5 where, compared to the model cloud fractions which show a pronounced peak around the smallest cloud fraction bin (compare Figure 3.16 lower panels), the lidar cloud fraction (Figures 3.16 top panel) has a much broader distribution with a local minimum in the smallest cloud fraction bin. Here we ask the question, to which extent this peak in the 1D observational data could be resulting from the sampling procedure.

#### *(a) The averaging process*

For convenience, we will not take the averages over distinct, non-overlapping grid boxes (or, similarly, non-overlapping 1D segments) as they are in an NWP model but, instead, averages will be taken as running means (which corresponds to a quasi-continuum of overlapping segments and grid boxes). Of course, statistically valid results are not changed by this procedure. Note that the corresponding 2D averages are constructed by taking two successive running means (in two different directions) or, in other words, by taking the running mean over the 1D averages (which had been constructed by taking a running mean).

#### *(b) The impact of the averaging on a PDF*

The averaging or coarse-graining of data sets leaves the mean invariant but decreases the variance. For single mode PDFs the main impact is generally a sharpening of the peak and for normally distributed variables the impact of the averaging process can be fully described by the corresponding changes of the variance. Since the averaging process can be written in form of the convolution with a weighting function, in its Fourier decomposition, changes to the variance can be written as the sum over simple products of Fourier components. Since, under the assumption of isotropy, the Fourier components can be estimated from the 1D measurements, the changes to the variance can also be estimated from the data.

While this method for computing changes to the variance is not restricted to Gaussian fields, for strongly non-Gaussian fields, changes of the variance can impact the PDF in very different ways, so that knowing the variance (or the changes to the variance) is not necessarily very conclusive for assessing the sampling error made when computing a PDF from 1D averages. As most of the cloud or precipitation related fields are strongly non-Gaussian, computations of the variance changes will not be presented here. Instead, observational data from the MODIS scanning satellite instruments are used to demonstrate the differences between 1D and 2D cloud fraction estimates. The main question we would like to answer is, in how far the CALIPSO cloud fraction PDFs presented in section 3.5 (for trade-cumulus clouds) are affected by the 1D sampling geometry.

A comparison between 1D and 2D averages of total cloud cover measured by MODIS is plotted in Figure 4.1. The data are taken over a region in the tropical Pacific (longitude  $\in [155 - 256]$ , latitude  $\in [20S - 20N]$ ) between the 1st and the 5th of July 2008. The overall mean cloud fraction of these data is 50% and the unaveraged field is binary with two equal sized peaks at zero and one. However, as can be seen from the top left graph of Figure 4.1, the asymmetry of these data becomes already obvious in the averages with the smallest averaging length (or area). For larger averaging domains, the peak near zero cloud fraction ( $a$ ) decreases gradually, and a comparably broad peak around  $a \in [0.2, 0.3]$  is formed.

The resulting PDF has a double peak structure and large part of the impact of increased averaging (i.e., of increasing the averaging length or going from 1D to 2D averages) can be divided into two (partially counteracting) aspects. On one hand, increasing the averaging length scale leads to a stronger mixing

between the two peaks. On the other hand, increased averaging can also sharpen individual peaks. This latter aspect is observed when going from 1D to 2D averages, with the small-cloud-fraction peak being generally sharper for the 2D averages (green curves in Figure 4.1).

In general, while being far from negligible, the differences between the 1D and 2D PDFs are in most regions never larger than 30%. The only exception to this is for very small cloud fractions for which the probability of occurrence vanishes quite quickly with increased averaging. The strong sensitivity of small cloud fractions to increased averaging can, however, also be seen from comparing only 1D averages but for different averaging lengths.

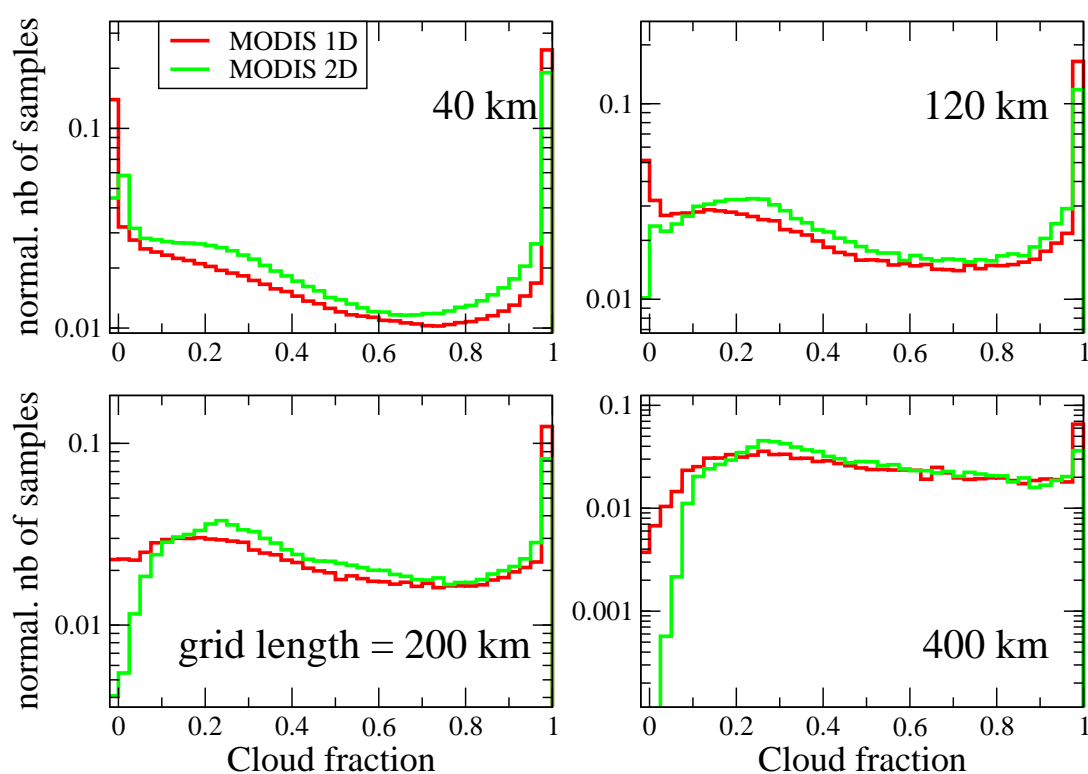


Figure 4.1: Number of samples in cloud fraction bins (normalised by the total number of samples) for MODIS 1km cloud fraction data averaged over line segments (red curves) and square section (green curves). Each graphs corresponds to a different averaging length (grid length) which is indicated (in km) in the respective graphs.

## 4.2 Measurement specifications

As explained above, the sampling error is not the only source of uncertainty when comparing models with observations (in the observation-to-model approach) but also the particular measurement specifications and sensitivities (and how they correspond to the use of the respective variable in an NWP model) have to be considered. Interesting in this context are the differences when comparing the MODIS results discussed above with the corresponding CALIPSO observations (total cloud cover computed from the 1km cloud layer product). As the two instruments have very different specifications and sensitivities such a comparison can be quite instructive.

Indeed, from Fig. 4.2 one sees that the difference between the PDFs obtained from CALIPSO (black squares) and MODIS (red curves) is quite striking and much larger than the MODIS 1D-2D differences discussed above. In the CALIPSO data, the small-cloud-fraction peak is much more pronounced for the

smaller averaging domains (see Figure 4.2) and occurs generally at much larger cloud fractions while the frequency of occurrence of smaller cloud fractions ( $a \in [0, 0.2]$ ) is dramatically reduced compared to the MODIS data. This is consistent with the fact that CALIPSO (with a mean cloud fraction of 60%) sees 20% more clouds than MODIS (whose mean cloud fraction of 50%).

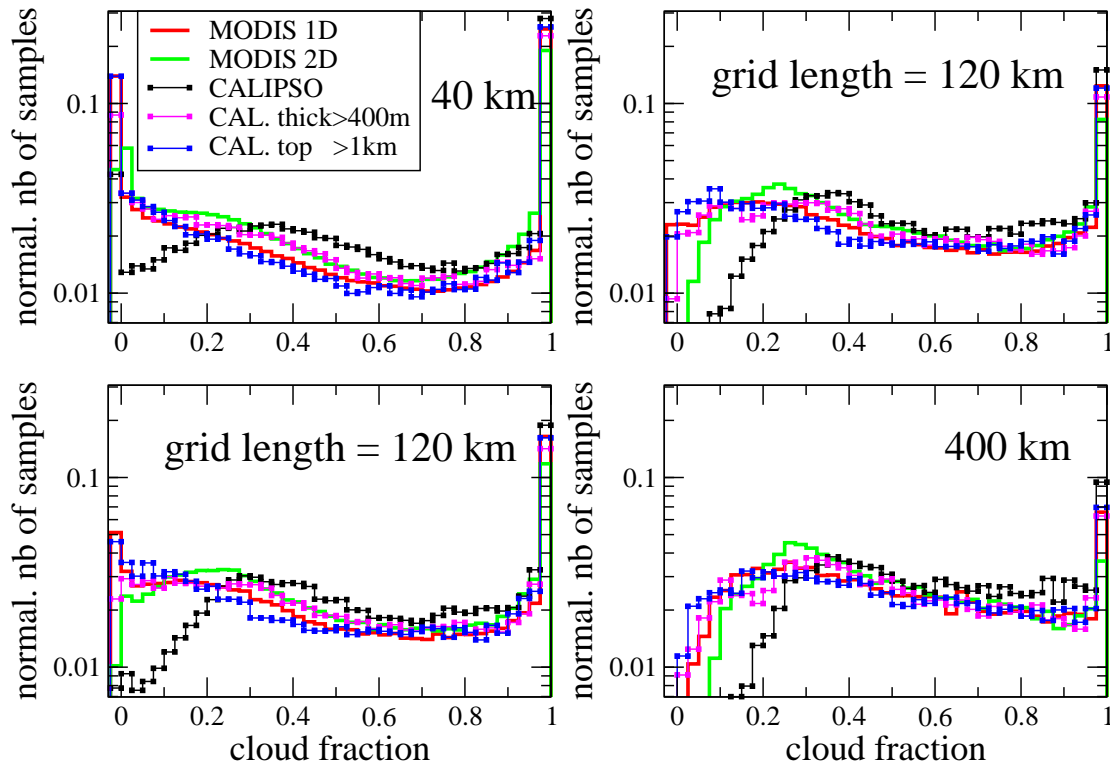


Figure 4.2: While the green and red curves are the same as in the top graphs of Figure 4.1, the black squares show the corresponding line averages obtained from CALIPSO data for a range of averaging length scales (“grid length”). For the coloured squares clouds detected by CALIPSO are only considered if their depth is either larger than 400 m (magenta squares) or if their cloud top is above 1km (blue squares), respectively.

The most probable explanation is that the CALIPSO lidar can see more low and/or optically thin clouds than MODIS sensors. A crude test how the restriction to thicker clouds alters the CALIPSO results is given by the magenta squares in Fig. 4.2. For these curves only clouds which are thicker than 400m have included (unless the lidar signal was attenuated). This restriction reduces the mean average cloud fraction to 50% (which is the same value as for the MODIS data). Also the resulting PDFs (magenta squares in Fig. 4.2) are substantially closer to that of the MODIS data (differences are in the same range as those between the 1D and 2D MODIS averages). Similar results are obtained by restricting CALIPSO clouds to those with cloud tops higher than 1km (blue squares in Fig. 4.2).

An interesting question is to what extent the thin clouds which MODIS can not see are relevant for the low clouds discussed in section 3.5. To investigate this, the CALIPSO statistics were recalculated for clouds with tops below 4km. As seen from Figure 4.3 the strong shift of the peak in the small cloud fraction regime (which results from the restriction to a minimum cloud-depth of 400m) is as clear as for the total cloud cover results (with no height restrictions) in Figure 4.2. That low clouds are, indeed, most relevant for the impact of the minimum cloud-depth criterion is shown in Figure 4.4 where this criterion has been applied, separately, only above (green curve) or only below (red curve) the 4 km level.

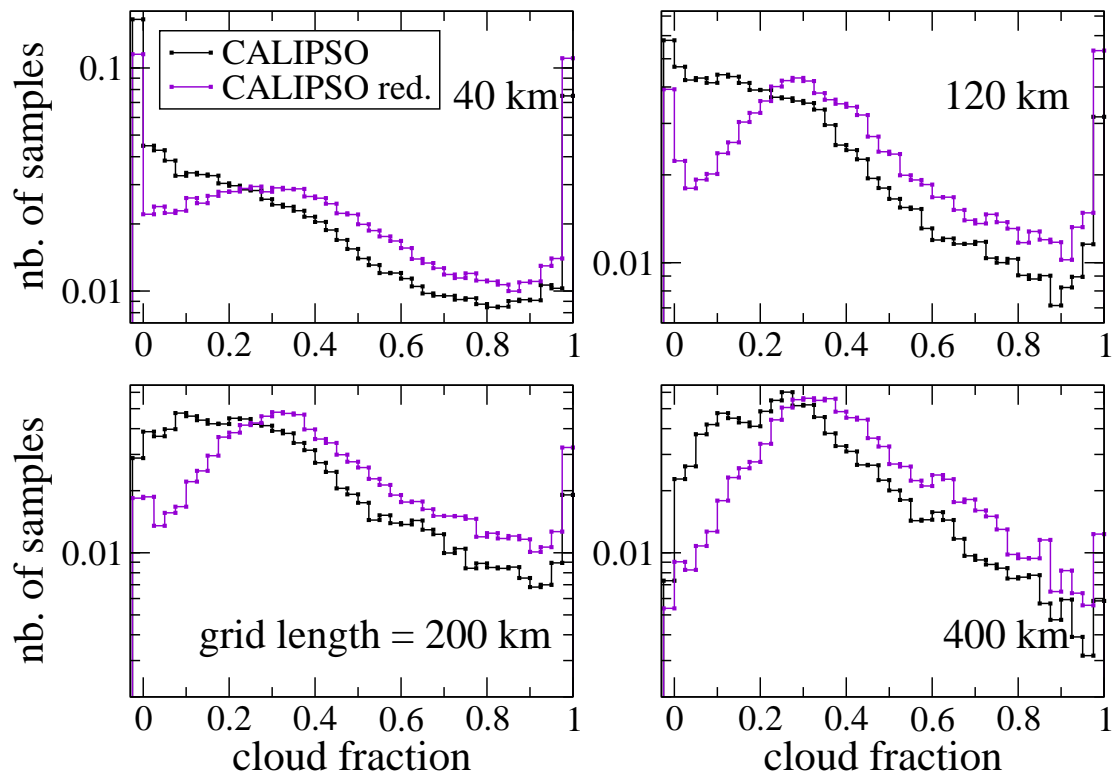


Figure 4.3: Number of samples in cloud fraction bins obtained from CALIPSO data (black line as shown on Fig. 4.2) and the same for clouds whose top does not exceed the height of 4 km (purple line).

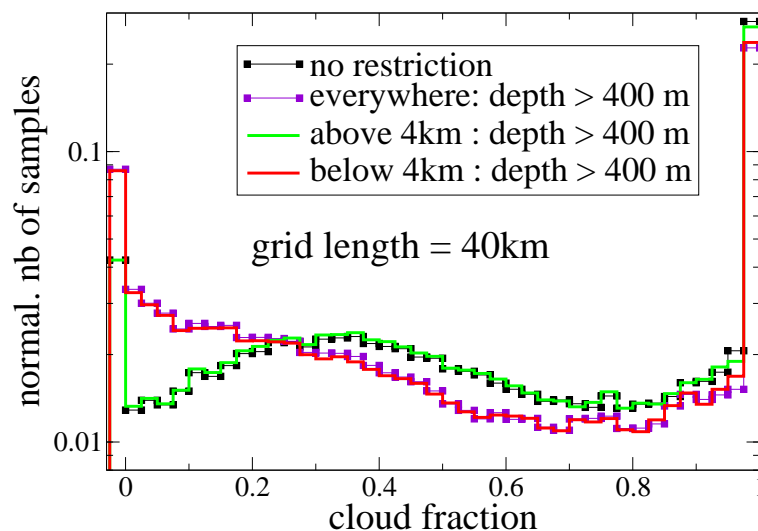


Figure 4.4: Cloud fractions obtained from CALIPSO 1km data averaged over 40km segments. As indicated in the legend, different restrictions have been applied for the different curves. While the black and violet square are the same as in the top graph of Figure 4.2, for the red and green curves, the restriction that clouds need to be more than 400m deep in order to be recognised has been applied only above (green curve) and below (red curve) the 4km level, respectively.

### 4.3 Conclusions and discussion of representativity issues

The results presented above illustrate that the small number in the smallest CALIPSO cloud-fraction bin, seen in the top panel of Figure 3.16 (which is in strong contrast to the corresponding model results shown in the middle and lower panels of Figure 3.16), is very likely *not* caused by sampling errors. On the contrary, the additional averaging (which converts 1D into 2D averages) is likely to sharpen the local peak at small (but non-zero) cloud fraction, as can be seen in Figure 4.1 for the MODIS data, for which the small cloud fraction peaks tend to be much more pronounced (and at slightly larger values) in the 2D than in the 1D averages. Similarly, averages taken over different size segments show that the peak at moderate cloud fractions in the CALIPSO data sharpens when the averaging domain is increased (see Figure 4.5). This is the typical behaviour expected for such a peak which indicates that this peak is not just an artifact of the smaller averaging related to the 1D sampling.

Calipso data averaged over different length scales

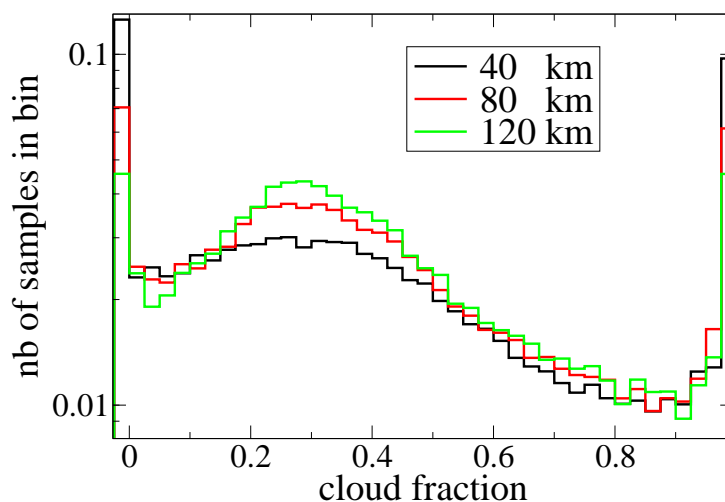


Figure 4.5: Distributions of cloud fractions obtained from CALIPSO 1km data when averaged over 40km, 80km and 120km segments as indicated in the legend.

The data presented in this section, however, indicate that the different forms of the modelled and observed cloud-fraction peaks (in the trade cumulus regime) found in section 3.5 could be linked to the existence of low and relatively thin clouds which CALIPSO can measure. This, also, raises a representativity problem, which, however, is not related to the sampling error. It raises the question to which extent the model is capable of representing such clouds. Particularly the representation of clouds whose vertical extent has the same magnitude or is smaller than its vertical resolution could be problematic. This issue illustrates the fact that representativity problems are not only related to shortcomings of the measurement processes (as, e.g., under-sampling) but, also, to the model's capability of representing reality on a model grid.

It should, however be noted, that possible difficulties of the model to represent thin clouds can not explain all of the differences between model and observations presented in section 3.5. Imposing a minimal cloud depth on CALIPSO data leads to a strongly decreased total cloud fraction (of the remaining clouds which fulfil the criterion), while in the data presented in section 3.5 the mean cloud fraction from the model and the unfiltered(!) CALIPSO data seemed to agree fairly well.

The findings of this section emphasise some of the possible problems which can be encountered when performing model-observation comparisons. One conclusion of this is that only strong discrepancies between modelled and observed data should be trusted and, also, that all results should be checked for different er-

ror sources. In this respect, the new active satellite instrument with their great vertical resolution offer us unprecedented possibilities for understanding observations more detailed by taking the vertical extent and height of clouds more explicitly into account. The investigations in subsection 2.2 give an example how this can help identifying error sources.

Of course, the small horizontal coverage of these instruments gives rise to a non-negligible sampling errors. In this respect, however, the differences between the 1D and 2D averages found in the MODIS data discussed above, were usually within a 30% range. Larger differences were found only in the range of very small cloud fraction (i.e., left of the the small cloud fraction peak) which in the 2D averages, decays much more rapidly. That the small cloud fraction range of the PDFs presented in this section is very sensitive to increased averaging can, however, be also seen when comparing 1D averages with different averaging length scales. Generally, It seems very likely that those parts of a PDF where sampling errors are potentially large can be identified by comparing different types of averages of the 1D data.

## 5 Conclusions

The question of how to evaluate a global NWP model with data from a space-borne radar and lidar, has been explored. Such validation studies require consideration of the problems of different parameters, different spatial scales and limitations/error characteristics of the observations. It is crucial to obtain a fair comparison between model and observations in order to identify real model performance and deficiencies, rather than artefacts of the representativity problem. One approach is to extract the data along the satellite track and forward-model the observed quantities (for example, simulated 94GHz attenuated radar reflectivity to compare with the CloudSat data). An alternative approach is to utilise the synergy of different remote sensing instruments and combine multiple observations to derive quantities predicted by the model (for example, ice water content from a retrieval of radar and lidar data). The spatial representativity issue can be at least partially addressed with appropriate averaging of the observations and use of the model predictions of sub-grid variability (cloud fraction), although a more promising approach is to use a cloud generator for each model grid point to produce a number of independent sub-columns consistent with the model sub-grid information. This can then be compared directly with the higher resolution observations. The representativity error of the pseudo-one-dimensional character of the observations versus the two-dimensional model grid boxes needs to be taken into account in certain circumstances (although it does not significantly affect the validation results described in this report). The evaluation process is not always straight forward and there is inevitably some uncertainty in the robustness of the model-observation comparisons. This is why it is important to approach the model evaluation from multiple angles, explore the sensitivity to uncertainties in the assumptions and understand the characteristics and limitations of both observation and model.

In order to improve the model parametrizations we need to evaluate the physical processes that lead to the atmospheric quantities of interest (in this case cloud and precipitation). Regime-dependent evaluation, focusing on a particular atmospheric phenomenon or regime, such as trade-cumulus where a limited number of physical processes are dominant, is a useful way forward. Breaking down the validation statistics into zonal regions is a first step in identifying cold cloud processes at high latitudes, mid-latitude storm tracks and tropical convection, but more selective criteria are required to isolate different regimes and this is a topic of future research. Model sensitivity studies can then indicate the contributions of different physical processes to the model performance.

The cloud occurrence validation in section 3.2 shows overall good agreement of the zonal distribution of cloud and precipitation occurrence. However, the comparison highlights some differences; lack of high level cloud in the tropics, over-prediction of low level cloud at high northern hemisphere latitudes and the generally higher frequency of occurrence of precipitation in the model at all latitudes. The latter may well be an artefact of the comparison as the frequency of occurrence of precipitation depends on the precipitation fraction which is an ill defined quantity in the model. Further investigation of the representation of precipitation fraction in the model is ongoing work.

The radar reflectivity comparison against CloudSat observations in section 3.3 shows both positive and negative aspects of the model cloud and precipitation field. The model has significant variability of radar reflectivity values for a given height, but less so than for the observations. There is an over-prediction of the frequency of hydrometeor occurrence in many areas. The over-occurrence of low-level rain in shallow convection (light precipitation) is a dominant feature. This result is supported by the precipitation comparison in section 3.6 which shows the occurrence of light precipitation ( $< 1$  mm/hr) in the model is over-estimated. The implications of the over-prediction of light precipitation is a topic for future research, but has potential impacts on the radiation and water cycle.

The ice water content (IWC) evaluation in section 3.4 shows the IWC values are generally too low but the frequency of occurrence is too high (consistent with the reflectivity comparison). These two factors could

be compensating to give a reasonable representation of the radiative impact of the cloud. The IWC from the new cloud scheme with prognostic snow and rain are in better agreement with the observations than the current diagnostic scheme. However, the new scheme enhances over-prediction of occurrence, again linked to the precipitation fraction of snow.

The oceanic trade-cumulus evaluation was an example for a particular cloud regime showing the good agreement of the spatial distribution of shallow convection in the model, but differences in the frequency and the cloud top height. The results also showed the improvement of the representation of the cloud top height for the oceanic trade cumulus regime with the new DualM parametrization for shallow cumulus.

Model developments over the next few years will lead to an increasingly complex representation of cloud and precipitation with the possibility of additional predicted variables representing different hydrometeor categories and information on the sub-grid variability (e.g. [Tompkins, 2002](#)). The process of model improvement combines information from a wide variety of observations, theory and experimentation across a range of modelling frameworks, leading eventually to improvement of operational NWP. It is therefore difficult to attribute particular improvements to a specific data source. However, the value of global datasets with high resolution vertical profiles of aerosol and cloud-related information (such as that from CloudSat/CALIPSO and EarthCARE) will provide an invaluable source of data to inspire and validate such model developments. The usefulness of space-borne radar and lidar data for validation of new parametrization developments at ECMWF has been highlighted in this work, in particular for the new version of the cloud scheme with additional prognostic variables for ice, liquid, rain and snow hydrometeors, and an extended version of the cloudy boundary layer scheme to improve the representation of shallow cumulus. Such data could be used to improve other aspects of the cloud parametrization including assumptions of sub-grid heterogeneity and assessment of model sensitivity to uncertain parameters in the representation of microphysics as two examples. The additional benefit of Doppler velocity from the EarthCARE satellite, if sufficiently sensitive will help to inform the model parametrization of ice and snow in the model. Therefore significant potential exists for future satellite-borne CPR/lidar sensors, such as EarthCARE, to further constrain and validate model parametrization schemes.

## Acknowledgements

The authors would like to acknowledge the NASA CloudSat Project for providing the CloudSat data, the NASA Langley Research Center Atmospheric Science Data Center for providing the CALIPSO data and the Goddard Earth Sciences Data and Information Services Center (GES DISC) for providing the MODIS data. The authors are very grateful to Graeme Stephens for discussions and collaboration on the analysis of precipitation products from CloudSat. The Atmospheric Radiation Measurement program supports a fellow at ECMWF (Grant No. DE-FG02-07ER64400), whose work contributed to the results presented in this report.

## A List of Acronyms

AWP	Amount when present
CFMIP	Cloud Feedback Model Intercomparison Project
COSP	CFMIP Observation Simulator Package
CPR	Cloud Profiling Radar
DualM	“Dual Mass Flux” parametrization scheme for shallow convection
ECMWF	European Centre for Medium-Range Weather Forecasts
EDMF	“Eddy-Diffusivity Mass Flux” boundary layer parametrization scheme
GCM	General (or Global) Circulation Model
IFS	Integrated Forecast System
IPCC	Intergovernmental Panel on Climate Change
ITCZ	Inter-Tropical Convergence Zone
IWC	Ice Water Content
IWP	Ice Water Path
LWP	Liquid Water Path
NH	Northern Hemisphere
NWP	Numerical Weather Prediction
PDF	Probability density function
SH	Southern Hemisphere
VFM	Vertical Feature Mask
ZmVar	ECMWF radar reflectivity forward model

## References

- Ahlgrimm, M., D. Randall, and M. Köhler, 2009: Evaluating cloud frequency of occurrence and top height using space-borne lidar observations, *Mon. Wea. Rev.*, **137**, 4225–4237.
- Bechtold, P., J.-P. Chaboureaud, A. Beljaars, A. K. Betts, M. Köhler, M. Miller, and J. L. Redelsperger, 2004: The simulation of the diurnal cycle of convective precipitation over land in a global model, *Quart. J. R. Meteorol. Soc.*, **130**, 3119–3137.
- Bechtold, P., M. Köhler, T. Jung, F. Doblas-Reyes, M. Leutbecher, M. J. Rodwell, F. Vitart, and G. Balsamo, 2008: Advances in simulating atmospheric variability with the ECMWF model: From synoptic to decadal time-scales, *Quart. J. R. Meteor. Soc.*, **134**, 1337–1351.
- Bodas-Salcedo, A., M. J. Webb, M. E. Brooks, M. A. Ringer, K. D. Williams, S. F. Milton, and D. R. Wilson, 2008: Evaluating cloud systems in the Met Office global forecast model using simulated CloudSat radar reflectivities, *J. Geophys. Res.-Atmospheres*, **113**(D00A13).
- Delanoë, J. and R. Hogan, 2009: Combined CloudSat-CALIPSO-MODIS retrievals of the properties of ice clouds, *Submitted to J. Geophys. Res.*.
- Delanoë, J. and R. J. Hogan, 2008: A variational scheme for retrieving ice cloud properties from combined radar, lidar, and infrared radiometer, *J. Geophys. Res.*, **113**(D07204).
- ECMWF, 2009: IFS Documentation CY33R1.
- Ferrier, B. S., 1994: A double-moment multiple phase four-class bulk ice scheme. Part 1: Description, *J. Atmos. Sci.*, **51**, 249–280.
- Fowler, L. D., D. A. Randall, and S. A. Rutledge, 1996: Liquid and ice cloud microphysics in the CSU GCM Part I: Model description and simulated microphysical processes, *J. Climate*, **9**, 489–529.
- Ghan, S. J., L. R. Leung, and Q. Hu, 1997: Application of cloud microphysics to NCAR community climate model, *J. Geophys. Res.*, **102**, 16507–16527.
- Gierens, K., U. Schumann, M. Helten, H. Smit, and A. Marengo, 1999: A distribution law for relative humidity in the upper troposphere and lower stratosphere derived from three years of MOZAIC measurements, in *Annales Geophysicae*, Springer, volume **17**, pp. 1218–1226.
- Haynes, J. M., T. S. L'Ecuyer, G. L. Stephens, S. D. Miller, C. Mitrescu, N. B. Wood, and S. Tanelli, 2009: Rainfall retrieval over the ocean with spaceborne W-band radar, *J. Geophys. Res.-Atmospheres*, **114**(D00A22, doi:10.1029/2008JD009973).
- Heymsfield, A. J., L. M. Miloshevich, C. Twohy, G. Sachse, and S. Oltmans, 1998: Upper-tropospheric relative humidity observations and implications for cirrus ice nucleation, *Geophys. Res. Lett.*, **25**(9), 1343–1346.
- Hogan, R. J., M. D. Behera, E. J. O'Connor, and A. J. Illingworth, 2004: Estimate of the global distribution of stratiform supercooled liquid water clouds using the LITE lidar, *Geophys. Res. Lett.*, **31**, L05106.
- Hogan, R. J., A. J. Illingworth, E. J. O'Connor, and J. P. V. Poiares-Baptista, 2003: Characteristics of mixed-phase clouds. II - A climatology from ground-based lidar, *Quart. J. R. Meteorol. Soc.*, **129**(592), 2117–2134.

- Ikawa, M., H. Mizuno, T. Matsuo, M. Murakami, Y. Yamada, and K. Saito, 1991: Numerical modeling of the convective snow cloud over the Sea of Japan. Precipitation mechanism and sensitivity to ice crystal nucleation rates, *J. Meteorol. Soc. Japan*, **69**, 641–667.
- Jakob, C. and S. A. Klein, 2000: A parametrization of the effects of cloud and precipitation overlap for use in general-circulation models, *Quart. J. R. Meteorol. Soc.*, **126**(568), 2525–2544.
- Köhler, M., 2005: A new PBL parameterization to improve low clouds in CY29R1, Research Department Memorandum 518, File:R.48.3/MK/0518.
- Köhler, M., 2005: Improved prediction of boundary layer clouds, *ECMWF Newsletter*, **104**, 18–22.
- Lin, Y., R. Farley, and H. Orville, 1983: Bulk parameterization of the snow field in a cloud model, *J. Appl. Meteor.*, **22**(6), 1065–1092.
- Matrosov, S. Y., P. T. May, and M. D. Shupe, 2006: Rainfall profiling using atmospheric radiation measurement program vertically pointing 8-mm wavelength radars, *J. Atmos. Oceanic Tech.*, **23**(11), 1478–1491.
- Morcrette, J.-J., H. W. Barker, J. N. S. Cole, M. J. Iacono, and R. Pincus, 2008: Impact of a New Radiation Package, McRad, in the ECMWF Integrated Forecasting System, *Mon. Wea. Rev.*, **136**, 4773–4798.
- Neggers, R. A. J., 2009: A Dual Mass Flux Framework for Boundary Layer Convection. Part II: Clouds, *J. Atmos. Sci.*, **66**, 1489–1506.
- Neggers, R. A. J., M. Khler, and A. C. M. Beljaars, 2009: A Dual Mass Flux Framework for Boundary Layer Convection. Part I: Transport, *J. Atmos. Sci.*, **66**, 1465–1487.
- Räisänen, P., H. W. Barker, M. F. Khairoutdinov, J. Li, and D. A. Randall, 2004: Stochastic generation of subgrid-scale cloudy columns for large-scale models, *Quart. J. R. Meteor. Soc.*, **130**, 2047–2067.
- Smith, R. N. B., 1990: A scheme for predicting layer clouds and their water content in a general circulation model, *Quart. J. R. Meteor. Soc.*, **116**, 435–460.
- Spichtinger, P., K. Gierens, and W. Read, 2003: The global distribution of ice-supersaturated regions as seen by the Microwave Limb Sounder, *Quart. J. R. Meteor. Soc.*, **129**(595), 3391–3410.
- Sundqvist, H., 1978: A parametrization scheme for non-convective condensation including prediction of cloud water content, *Quart. J. R. Meteor. Soc.*, **104**, 677–690.
- Sundqvist, H., E. Berge, and J. E. Kristjánsson, 1989: Condensation and cloud paranetrization studies with a mesoscale numerical weather prediction model, *Mon. Wea. Rev.*, **117**, 1641–1657.
- Swann, H., 1998: Sensitivity to the representation of precipitating ice in CRM simulations of deep convection, *Atmos. Res.*, **47/48**, 415–435.
- Tiedtke, M., 1989a: A comprehensive mass flux scheme for cumulus parameterization in large-scale models, *Mon. Wea. Rev.*, **117**, 1779–1800.
- Tiedtke, M., 1989b: A comprehensive mass flux scheme for cumulus parameterization in large-scale models, *Mon. Wea. Rev.*, **117**, 1779–1800.
- Tiedtke, M., 1993: Representation of clouds in large-scale models, *Mon. Wea. Rev.*, **121**, 3040–3061.
- Tompkins, A. M., 2002: A prognostic parametrization for the subgrid-scale variability of water vapor and clouds in large-scale models, *J. Atmos. Sci.*, **59**, 1917–1942.

- Tompkins, A. M., P. Bechtold, A. C. M. Beljaars, A. Benedetti, S. Cheinet, M. Janisková, M. Köhler, P. Lopez, and J.-J. Morcrette, 2004: Moist physical processes in the IFS: Progress and plans, ECMWF Technical Memorandum 452, 91 pp.
- Tompkins, A. M., K. Gierens, and G. Radel, 2007: Ice supersaturation in the ECMWF integrated forecast system, *Quart. J. R. Meteor. Soc.*, **133**, 53–63.
- Waliser, D. E., J. L. F. Li, C. P. Woods, R. T. Austin, J. Bacmeister, J. Chern, A. Del Genio, J. H. Jiang, Z. Kuang, H. Meng, *et al.*, 2009: Cloud ice: A climate model challenge with signs and expectations of progress, *J. Geophys. Res.-Atmospheres*, **114**(D00A21, doi:10.1029/2008JD010015).
- Walko, R. L., W. R. Cotton, M. P. Meyers, and J. Y. Harrington, 1995: New RAMS cloud microphysics parameterization. Part I. The single-moment scheme, *Atmos. Res.*, **38**, 29–62.
- Wang, C. and J. S. Chang, 1993: A three-dimensional model of cloud dynamics, microphysics and chemistry, 1. Concepts and formulation, *J. Geophys. Res.*, **98**, 14827–14844.
- Wilson, D. R. and S. P. Ballard, 1999: A microphysical based precipitation scheme for the UK Meteorological Office numerical weather prediction model, *Quart. J. Roy. Meteor. Soc.*, **125**, 1607–1636.